

AD _____

Award Number: W81XWH-07-1-0708

TITLE: Design, Fabrication, Characterization and Modeling of Integrated Functional Materials

PRINCIPAL INVESTIGATOR:

Pritish Mukherjee, Ph. D.
Hariharan Srikanth, Ph. D.
Sarath Witanachchi, Ph. D.
George Nolas, Ph. D.

CONTRACTING ORGANIZATION: University of South Florida
Tampa, FL 33620, USA

REPORT DATE: October 2009

TYPE OF REPORT: Annual Report

PREPARED FOR: U.S. Army Medical Research and Materiel Command
Fort Detrick, Maryland 21702-5012

DISTRIBUTION STATEMENT:

X Approved for public release; distribution unlimited

The views, opinions and/or findings contained in this report are those of the author(s) and should not be construed as an official Department of the Army position, policy or decision unless so designated by other documentation.

REPORT DOCUMENTATION PAGE			<i>Form Approved</i> <i>OMB No. 0704-0188</i>		
Public reporting burden for this collection of information is estimated to average 1 hour per response, including the time for reviewing instructions, searching existing data sources, gathering and maintaining the data needed, and completing and reviewing this collection of information. Send comments regarding this burden estimate or any other aspect of this collection of information, including suggestions for reducing this burden to Department of Defense, Washington Headquarters Services, Directorate for Information Operations and Reports (0704-0188), 1215 Jefferson Davis Highway, Suite 1204, Arlington, VA 22202-4302. Respondents should be aware that notwithstanding any other provision of law, no person shall be subject to any penalty for failing to comply with a collection of information if it does not display a currently valid OMB control number. PLEASE DO NOT RETURN YOUR FORM TO THE ABOVE ADDRESS.					
1. REPORT DATE 01-10-2009		2. REPORT TYPE Annual		3. DATES COVERED 20 Sep 2008 to 19 Sep 2009)	
4. TITLE AND SUBTITLE Design, Fabrication, Characterization and Modeling of Integrated Functional Materials			5a. CONTRACT NUMBER		
			5b. GRANT NUMBER W81XWH-07-1-0708		
			5c. PROGRAM ELEMENT NUMBER		
6. AUTHOR(S) PI: Pritish Mukherjee, Ph. D. co-PIs: Hariharan Srikanth, Ph.D.; Sarath Witanachchi, Ph. D.; George Nolas, Ph. D.			5d. PROJECT NUMBER		
			5e. TASK NUMBER		
			5f. WORK UNIT NUMBER		
7. PERFORMING ORGANIZATION NAME(S) AND ADDRESS(ES) University of South Florida Tampa, FL 33620, USA			8. PERFORMING ORGANIZATION REPORT NUMBER		
9. SPONSORING / MONITORING AGENCY NAME(S) AND ADDRESS(ES) U.S. Army Medical Research and Materiel Command Fort Detrick, Maryland 21702-5012			10. SPONSOR/MONITOR'S ACRONYM(S)		
			11. SPONSOR/MONITOR'S REPORT NUMBER(S)		
12. DISTRIBUTION / AVAILABILITY STATEMENT Approved for public release; distribution unlimited					
13. SUPPLEMENTARY NOTES					
14. ABSTRACT The dynamically evolving needs of the U.S. soldier in the battlefield in response to changes in the technology of warfare and associated threats require advances in multiple areas including biomedical diagnostics, chemical sensing, communication technology, efficient power generation without increased payload, and mobile refrigeration. These technological advances are critically dependent on the development of new and currently non-existing materials. This research addresses the directed development of novel materials towards long-term needs of the United States Army. In order to address specific areas of integrated functional materials targeted towards the needs of the U.S. soldier in the field we have initiated research efforts in three main areas which are diagnostics and sensing, communication and energy, and power generation and refrigeration. The specific three independent "Tasks" that have been undertaken are: Task I: Nanostructured materials for biomedical diagnostics and chemical sensing Task II: Multifunctional composites for communication and energy applications Task III: Solid-state materials for power generation and refrigeration The specific outcome of the research activities is expected to lead to new devices/systems/composite materials useful for the USAMRMC.					
15. SUBJECT TERMS Functional materials, integrated fabrication, nanobiotechnology, smart materials, multifunctional, dimensional integration, nanocomposites, sensor technology, thermoelectrics, solar cells, photovoltaics					
16. SECURITY CLASSIFICATION OF:			17. LIMITATION OF ABSTRACT UU	18. NUMBER OF PAGES 59	19a. NAME OF RESPONSIBLE PERSON USAMRMC
a. REPORT U	b. ABSTRACT U	c. THIS PAGE U			19b. TELEPHONE NUMBER (include area code)

Design, Fabrication, Characterization and Modeling of Integrated Functional Materials
(Program Director and PI: Prof. Pritish Mukherjee, Department of Physics, USF, Tampa, FL)
(co-PIs: Profs. Hariharan Srikanth, Sarath Witanachchi and George Nolas)

Table of Contents

	<u>Page</u>
I. Introduction.....	4
II. Technical Description of Research Progress.....	7
III. Reportable Outcomes.....	53
IV. Conclusion.....	57
V. Bibliography.....	58

Design, Fabrication, Characterization and Modeling of Integrated Functional Materials

(Program Director and PI: Prof. Pritish Mukherjee, Department of Physics, USF, Tampa, FL)

(co-PIs: Profs. Hariharan Srikanth, Sarath Witanachchi and George Nolas)

I. Introduction

The dynamically evolving needs of the U.S. soldier in the battlefield in response to changes in the technology of warfare and associated threats require advances in multiple areas including biomedical diagnostics, chemical sensing, communication technology, efficient power generation without increased payload, and mobile refrigeration. These technological advances are critically dependent on the development of new and currently non-existing materials. This research addresses the directed development of novel materials towards long-term needs of the United States Army.

Objective:

In addition to the integration of multiple functionalities with desirable properties (thermal, electrical, magnetic, mechanical, optical, etc.), the connection to real-world applications and devices also requires the seamless integration of dimensions (nano, micro, meso, macro) leading to integrated functional materials. We have initiated this Integrated Functional Materials Project at the Physics Department at the University of South Florida (USF) geared towards precisely addressing this grand challenge of dual integration. A series of targeted projects specifically address a spectrum of issues relevant to the needs of the U.S. soldier.

Specific Aims:

The Physics Department at the University of South Florida is home to a unique doctoral program in Applied Physics with an affiliated industrial practicum and nationally recognized research programs in physical and chemical materials synthesis and characterization of bulk materials, thin films and nanomaterials; crystal fiber growth; fundamentals of materials manufacturing processes and computational theoretical materials physics. This research synergistically coalesces existing expertise and leverages research infrastructure at USF in novel bulk materials synthesis, thin film growth, and nanotechnology. These goals are being further addressed through multidisciplinary research and new infrastructure development. The basic purpose of this project is to develop the novel science base both in the areas of multi-scale dimensional integration as well as multiple functional integration leading to previously unattained integrated functional materials.

Study Design:

In order to address specific areas of integrated functional materials targeted towards the needs of the U.S. soldier in the field we are directing the research efforts in three main areas which are diagnostics and sensing, communication and energy, and power generation and refrigeration. The specific three independent “Tasks”, further subdivided into seven “Projects” are:

Task I: Nanostructured materials for biomedical diagnostics and chemical sensing***(Technical Directors.: Drs. H. Srikanth and P. Mukherjee)***

- Project 1* Functional magnetic fluids for biomedical applications
- Project 2* Nanoporous/nano-wire structures and polymer nanotemplates for sensing and molecular manipulation
- Project 3* Carbon-nanotube based sensors
- Project 4* Functional materials for affecting cell proliferation and locomotion

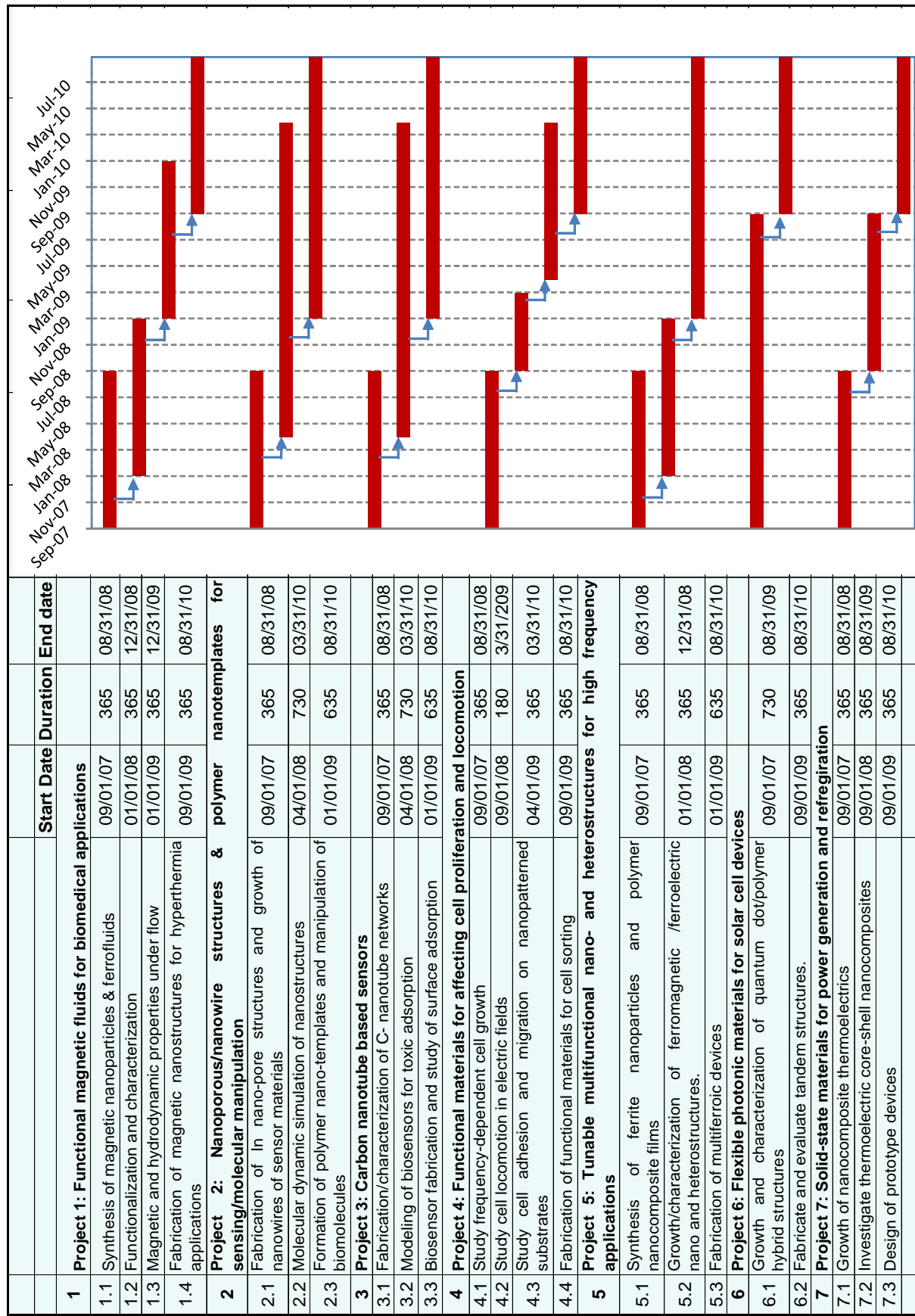
Task II: Multifunctional composites for communication and energy applications***(Technical Director: Dr. S. Witanachchi)***

- Project 5* Tunable multifunctional nano- and heterostructures for RF and microwave applications
- Project 6* Flexible photonic materials for solar-based energy sources

Task III: Solid-state materials for power generation and refrigeration***(Technical Director: Dr. G. S. Nolas)***

- Project 7* High-performance nanofabricated thermoelectric materials for power generation and refrigeration

The timeline for proposed activities for each of these projects (over the three-year period of research) is detailed in the Gantt chart on the following page.



II. Technical Description of Research Progress

The following discussion details the progress made on each of the Tasks during the second year of research:

Task I: Nanostructured materials for biomedical diagnostics and chemical sensing

Functional magnetic fluids for biomedical applications: synthesis and magnetic properties of ferrofluids

The goal of this project is to synthesize and characterize ferrofluids that would serve as biocompatible carriers for targeted drug delivery. Ms. Marienette Morales was supported as a Research Assistant through summer 2009. She graduated with an M.S. degree in June 2009. A new Ph.D. student Mr. Sayan Chandra has joined the project and is being supported as an RA from August 2009. In addition, undergraduate student Ms. Kristen Stojak assisted the team with aspects of synthesis of nanoparticles and polymer nanocomposites. Postdoctoral research associate Dr. Susmita Pal has continued her contributions to all projects in Task I. In year 2, fundamental studies of magnetic fluids continued and we obtained substantial insights into the particle size dependence. Work also progressed on polymer nanocomposites with uniformly dispersed nanoparticles and we have started to explore a novel biosensing method based on giant magneto-impedance (GMI). Graduate student Mr. Anurag Chaturvedi and postdoctoral researcher Dr. Manh-Huong Phan have assisted with this aspect of the project.

Tuning the magnetism in ferrofluids through size dependence of nanoparticles

We have continued our research understanding the effect of blocking temperature (T_B) of ferrofluids and the interaction of the particles by varying the carrier liquid and also by varying the particle size. We had earlier synthesized 14 nm Fe_3O_4 and 11nm $CoFe_2O_4$ nanoparticles by chemical co-precipitation route. The nanoparticles were dispersed in two different solvents; hexane and dodecane, having different viscosities and freezing temperatures. The carrier liquids were chosen such that the blocking temperature of nanoparticles (179K) was above the freezing temperature of hexane (178K) and below that of dodecane (264K). From the field-cooled and zero-field-cooled magnetization curves (FC-ZFC), a sharp peak was observed at T_B for the Fe_3O_4 based ferrofluids ($T_B < T_F$), while a magnetic anomaly (i.e., a sharp drop in the ZFC magnetization at low temperature) was observed for $CoFe_2O_4$ based ferrofluids ($T_B > T_F$). The occurrence of the two peaks was further verified from the complex susceptibility data, where the imaginary part $\chi''(T)$ showed single peak for ferrofluids having $T_B < T_F$, while the ferrofluids having $T_B > T_F$ had two peaks. The presence of the second peak in $\chi''(T)$ is ascribed to the blocking of magnetic nanoparticles, while the first peak in $\chi''(T)$ is associated with the freezing of the solvent. The ferrofluids were found to have interacting particles, with acceptable fit parameters within the Vogel-Fulcher model. From the $\chi'(f)$ plot it was found that for ferrofluids having $T_B > T_F$, Brownian and Neel relaxation co-existed in the mixed state while in the frozen state, only Neel relaxation was observed. However, for ferrofluids having $T_B < T_F$ Brownian and Neel relaxation co-existed in both the mixed state and the frozen state.

The physical origin of relaxation peaks in the complex susceptibility and the spin-glass-like cusp and magnetic anomaly in the zero-field-cooled (ZFC) magnetization depends on whether the particle blocking and carrier fluid freezing temperatures are close or far apart from

each other. In order to further understand how the difference in T_B and T_F affects the interparticle interactions, we successfully synthesized 6 nm and 10nm Fe_3O_4 nanoparticles. A comparative systematic study of 6nm, 10nm and 14nm ferrofluids would give us insight on the behavior of interactions of the nanoparticles based on how far the blocking temperatures of the nanoparticles are from the freezing temperature of carrier solvent.

The method of synthesizing ferrofluids consists of preparation of magnetic nanoparticles and the subsequent stabilization of the surfactant-coated nanoparticles in different nonpolar solvents. Fe_3O_4 nanoparticle synthesis was carried out using chemical coprecipitation process. Fe (III) acetylacetonate (2 mmol) and 1, 2-hexadecanediol (10 mmol) were added to 20 ml benzyl ether while stirring vigorously. The particles are coated with oleylamine (6 mmol) and oleic acid (6 mmol). The mixture is heated to $200^{\circ}C$ for 2 hours under argon environment and then allowed to reflux for 1 hour at $300^{\circ}C$. After cooling down to room temperature, the resulting black mixture is washed by adding 40 ml of ethanol. The black precipitate is extracted after centrifugation and magnetic decantation. The nanoparticles are then dissolved in hexane containing 1 drop each of oleic acid and oleylamine to ensure that nanoparticles are fully coated. Fe_3O_4 nanoparticles are stored in hexane liquid. To prepare the ferrofluids, measured amounts of the powder obtained by evaporation of carrier liquid were redispersed in hexane and in dodecane.

The experiments for 6nm NPs were performed on 3 samples: (a) Fe_3O_4 powder, (b) Fe_3O_4 + hexane and (c) Fe_3O_4 + dodecane. Each ferrofluid contains 2 vol% of Fe_3O_4 nanoparticles. In order to determine the composition and structure, XRD spectra using a Bruker D8 diffractometer was recorded for the powder sample. The shape and size distribution of the nanoparticles were determined using a Morgagni 280 transmission electron microscopy (TEM), after evaporation of very dilute fluid sample. DC magnetization measurements were done using Physical Property Measurement system (PPMS) with an applied field of 100 Oe. The temperature dependence of the complex AC susceptibility were obtained using measuring frequencies of 10 Hz, 50 Hz, 100 Hz, 500 Hz and 1 kHz.

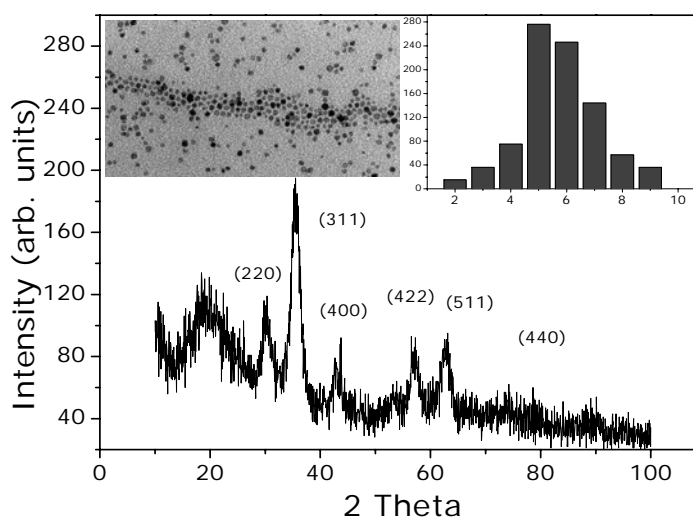


Figure 1: X-ray powder diffractogram of Fe_3O_4 sample. The insets display a histogram of nanoparticle size distribution and a TEM image for the same sample.

Figure 1 shows XRD and TEM images of the 6nm NPs. It can be seen that the NPs have narrow size distribution. Figure 2 depicts the zero field-cooled (ZFC) and field-cooled (FC) curves for (a) powder (b) Fe_3O_4 +hexane (c) Fe_3O_4 +dodecane. A sharp peak at 35 K is the blocking temperature of the powder sample. This illustrates the nanoparticles' narrow size distribution. The T_B of Fe_3O_4 +hexane (Figure 2b) occurs at 18 K, which is much lower than the blocking temperature of the nanoparticles in powder form at 35 K. This is expected since the inter-particle separation increases when the nanoparticles are dispersed in a liquid medium. On the bottom panel, we obtain 19 K for T_B of Fe_3O_4 +dodecane. Compared to that of the hexane sample, it is slightly higher but still much lower than the blocking temperature of pure Fe_3O_4 powder. We can see from Fig. 2 that no magnetic anomaly is observed in the ZFC plot for Fe_3O_4 + dodecane ferrofluid as was seen for the 14nm sample reported earlier. This was expected since $T_B < T_F$ for this ferrofluid, but the absence can be attributed to minimum or no interaction between the nanoparticles.

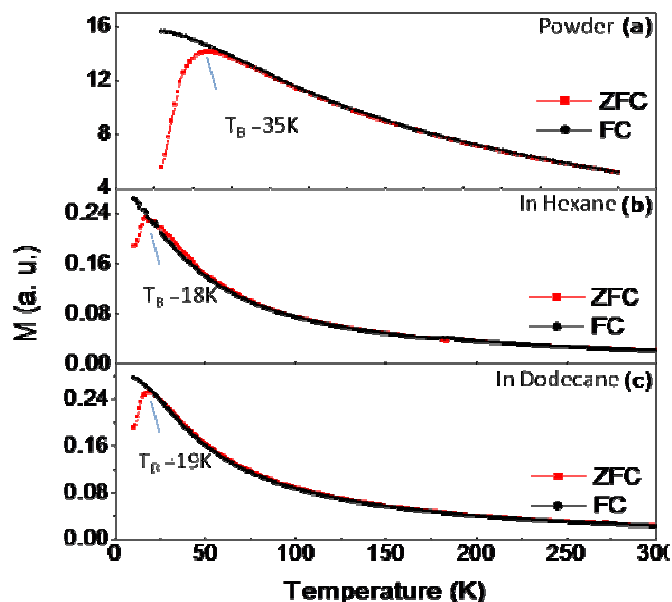


Figure 2: Zero field-cooled - field-cooled curves of (a) Fe_3O_4 powder (b) Fe_3O_4 +hexane (c) Fe_3O_4 +dodecane.

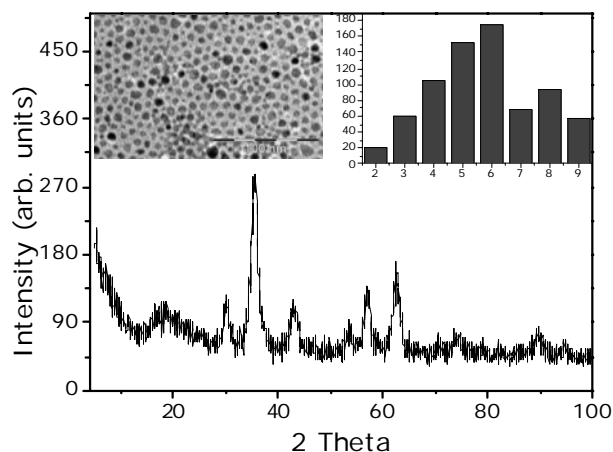


Figure 3: X-ray powder diffractogram of CoFe_2O_4 sample. The insets display a histogram of nanoparticle size distribution and a TEM image for the same sample.

This indicates that the viscosity of the solvent also plays a role in the behavior of the ferrofluids. Our finding is important from the technological application perspective since the application of a magnetic field to a ferrofluid is shown to significantly change the viscosity that in turn modifies the magnetic behavior of the ferrofluid. A similar set of experiments were done with 6nm CoFe_2O_4 -based ferrofluids. The nanoparticles were prepared by chemical co-precipitation method. Two different ferrofluids were prepared by dispersing the nanoparticles in hexane and dodecane, 2% by volume. Figure 3 shows the TEM image of the nanoparticles prepared, and very little distribution in size is observed.

The ZFC and FC magnetization curves of all the samples investigated are shown in Figs. 4. T_B for the powder sample is 254K. CoFe_2O_4 + hexane and CoFe_2O_4 + dodecane have blocking temperatures of 198K and 235K respectively. There is considerable decrease in T_B of

the ferrofluids similar to that observed for the 6nm Fe_3O_4 -based ferrofluids. The sharp peak in Figure 4(b) is due to the combined effect of the blocking of nanoparticles and the freezing of hexane. A second peak is present in Figure 4(c) which can be attributed to the freezing of dodecane. The absence of a second peak in CoFe_2O_4 + hexane is because the viscosity of hexane is less than dodecane. No magnetic anomaly is seen in the CoFe_2O_4 + dodecane sample which suggests that there is no interaction between the nanoparticles similar to that observed for the 6nm Fe_3O_4 based ferrofluids. Recall that we had earlier reported the presence of magnetic anomaly in the 11nm CoFe_2O_4 + dodecane sample.

Overall, our continued investigations of the particle size effects in ferrofluids have resulted in better understanding of the physical properties of these systems. While from the perspective of research, the focus was on nanoparticles dispersed in organic solvents, we have also demonstrated water-based magnetic nanoparticles that are biocompatible. New results on these systems will be presented in a later section of this report.

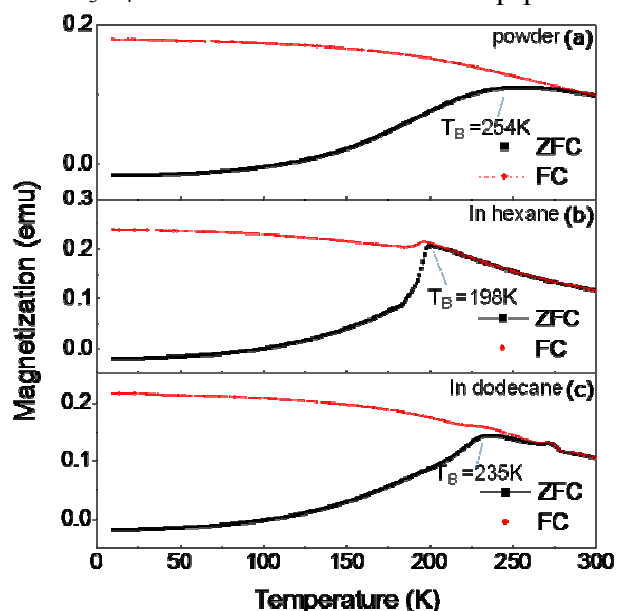


Figure 4: Field-cooled - field-cooled curves of (a) CoFe_2O_4 powder (b) CoFe_2O_4 +hexane (c) CoFe_2O_4 +dodecane.

Magnetic polymer nanocomposites

Polymer nanocomposites are very useful for applications in sensors and biomedicine because of their versatile electrical, thermal, mechanical, and optical properties. However, uniform dispersion of nanoparticles into a polymer matrix has been a bottleneck for nanocomposite fabrication. One of the best ways is to functionalize the particle surface with organic surfactants. The polymer matrix and inorganic particles often possess different polarities. Simple blending of particles with polymer will result in aggregates of particles because of particle diffusion. If the particles are surface functionalized with organic surfactants, their diffusion is minimized and also compatibility with the polymer matrix is enhanced resulting in a homogeneous dispersion of nanoparticles. Many types of organic compounds were used as surfactants to functionalize the nanoparticle surface, such as thiol, pyridine, carboxylic acids, and so forth. We report on a polymer mediated self assembly of magnetic nanoparticles and are currently studying their structural, magnetic properties and microwave response for sensor and tunable device applications. In this report, we briefly describe the synthesis and properties of cobalt ferrite (CoFe_2O_4) nanoparticles dispersed in a low-loss commercial polymer matrix obtained from Rogers Corporation.

2 mmol of Cobalt (II) acetylacetonate [$\text{Co}(\text{acac})_2$] and Iron (III) acetylacetonate [$\text{Fe}(\text{acac})_3$] were mixed in 1:2 ratio. 10 mmol 1,2-hexadecanediol, 6 mmol oleic acid, 6 mmol oleylamine and 20 ml benzyl ether were added to the Iron (III) acetylacetonate and Cobalt (II) acetylacetonate mixture. The mixture was stirred magnetically under a flow of argon, heated to 200 °C for 2 hours, and then refluxed at 300 °C for another 1 hour in presence of argon. The

reaction mixture was cooled to room temperature by removing the heat source. Under ambient conditions, 40 ml ethanol was added to the mixture and a black precipitate was separated by centrifugation. The black product was dissolved in hexane in presence of oleic acid (~ 0.05 ml) and oleylamine (~ 0.05 ml) and centrifuged to remove the undispersed residue. The product of 8nm CoFe_2O_4 particle was then precipitated with ethanol, centrifuged to remove the solvent and re-dispersed into hexane. The as-synthesized CoFe_2O_4 was dried in room temperature. The dried CoFe_2O_4 was added to the hexane solution of Rogers polymer by 16 and 33 wt% ratio. The polymer nanocomposites were dried at 140°C for 3 h. We have characterized these samples by XRD and TEM and magnetic characterizations were done in our Physical Property Measurement System.

The XRD pattern (Fig. 5a) of as-synthesized nanoparticles was consistent with the cubic structure of CoFe_2O_4 . The particle size, shape and distribution were determined from TEM imaging (Fig. 5b, 5c). The particle size of the CoFe_2O_4 was estimated to be about $8\text{ nm} \pm 2\text{ nm}$. The TEM images of polymer nanocomposites show that particles are uniformly embedded into the Rogers polymer matrix. We have made $20\mu\text{m}$ thick film of the nanocomposites for

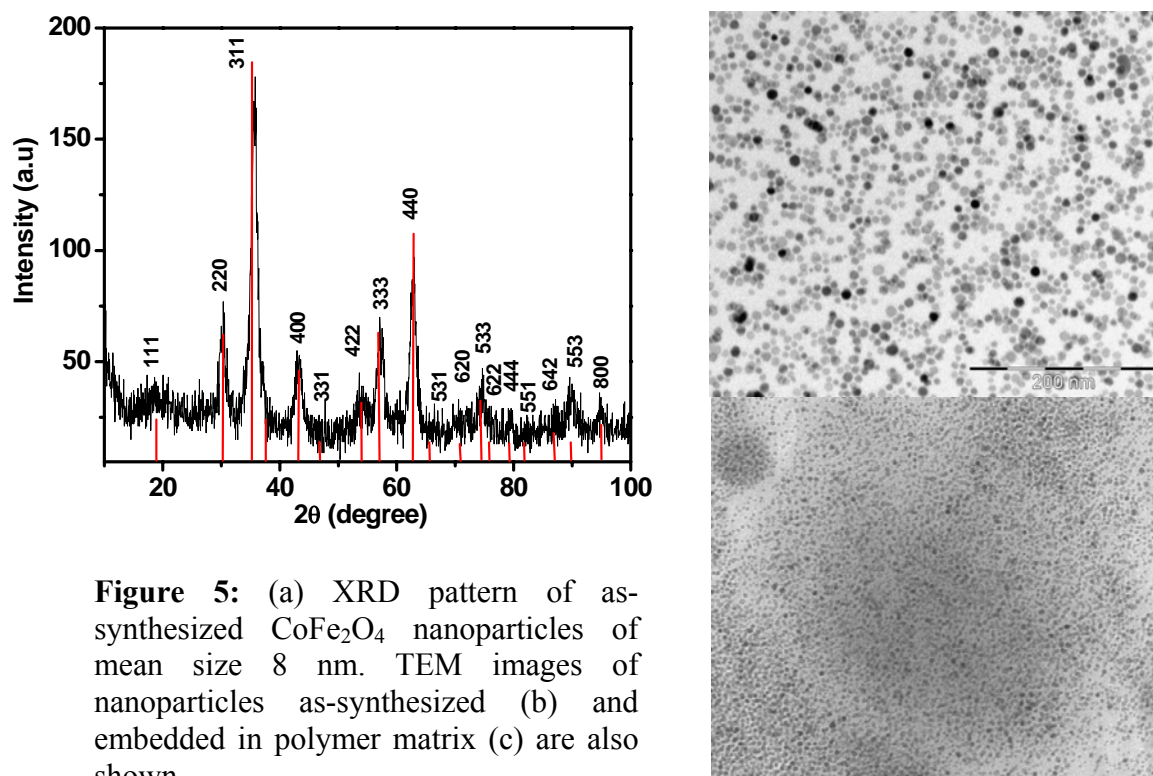


Figure 5: (a) XRD pattern of as-synthesized CoFe_2O_4 nanoparticles of mean size 8 nm. TEM images of nanoparticles as-synthesized (b) and embedded in polymer matrix (c) are also shown

electromagnetic sensor development. The entire thick film has excellent dispersion of the particles and magnetic properties confirm that these films exhibit nanomagnetic response useful for applications.

The M-T measurements (Fig 6) at 100 Oe using the standard zero-field cooled (ZFC) and field-cooled (FC) modes for all the samples show the characteristic behavior of isolated

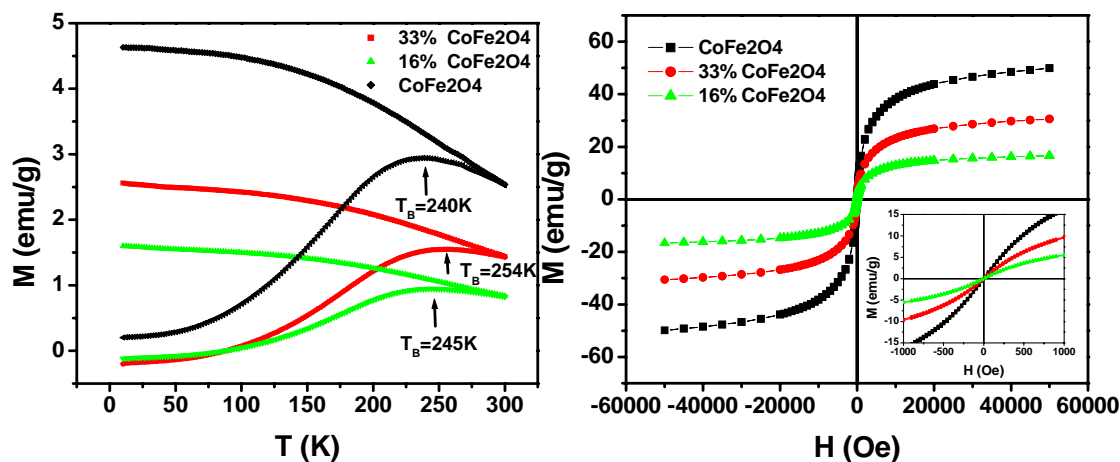


Figure 6: (Left) Temperature dependent magnetization curves (M-T) for the as-synthesized nanoparticles and two polymer nanocomposite films with different wt% loading of particles into Rogers polymer matrix (Right) M-H curves at room temperature indicating no coercivity consistent with superparamagnetic response. Inset shows the low-field region.

nanoparticles with a blocking temperature around 250K. There is a slight increase in blocking temperature in the polymer nanocomposites which is expected from an increase in inter-particle interactions.

The most important magnetic response is shown in the right panel of Figure 6. The as-synthesized nanoparticles along with the two different thick polymer nanocomposite films show identical shapes of the M-H loops (albeit with different saturation magnetization values) at room temperature, without any trace of coercivity. This is a significant result because it proves that the entire large area film behaves as a nanomagnetic system exhibiting classic superparamagnetic response. Lack of coercivity would imply no magnetic losses and thus desirable for low loss, frequency tunable electromagnetic sensing applications. In future studies, we will investigate the microwave absorption properties of these films and demonstrate tunable response for sensors.

Giant magneto-impedance based sensing of biocompatible fluids

Ferrofluids are potentially important materials for biomedical applications, such as cancer treatment either by hyperthermia using the change of magnetization in an AC magnetic field to heat the tissue, or by drug targeting [1]. In this case, it is necessary to use an external magnetic field to sense cells that have taken up magnetic nanoparticles. This technique is widely known as a magnetic biosensing technique (or a magnetic biosensor). For this application, a low-cost, reliable, highly sensitive and rapid sensor is required.

We have started developing a new type of biosensor based on the giant magnetoimpedance (GMI) effect [2]. The large magnitude of GMI effect observed in a number of soft ferromagnetic materials, together with a very high sensitivity at low fields, lack of hysteresis and high temperature stability holds great promise in field sensing. It has been shown that GMI-based sensors are superior to other sensors (e.g. GMR and Hall sensors), since they are more sensitive to low magnetic fields and present smaller power dissipation per unit area. This type of sensor has proven useful for biomolecular detection [3,4]. Recently, we have successfully

employed the GMI effect of Co-based amorphous magnetic ribbons to detect the presence of human embryonic kidney (HEK 293) cells loaded with Fe_3O_4 nanoparticles [5]. This method, in which the impedance of the magnetic ribbon changes with the DC magnetic field, relies on the fringe fields associated with the magnetic nanoparticles inside the cells to give a change in magnetoimpedance from the normal response exhibited by the ribbons. Although GMI sensors are very promising for biosensing technology, their development is still at the early stage. An emerging issue has remained unsolved regarding the detecting mechanism of a GMI sensor for low magnetic signals from magnetic markers (magnetic nanoparticles) as these particles are dispersed in a liquid media. To address this important issue, it is essential to study: the possibilities of sensing magnetic nanoparticles at different concentrations, size, magnetic moments distributions of the particles; the signal-to-noise ratio as a function of an active sensor area and temperature; and to check the ability of binding affinity measurements in living systems starting in the beginning with synthetic bioreceptors as a model system.

In our initial studies, we have investigated the GMI effect of the Co-based magnetic ribbon in the absence and presence of Fe_3O_4 -based ferrofluid over the frequency range of 0.5 Hz – 13 MHz. Our preliminary results have revealed GMI as a new electrochemical probe of the electric features of surface-modified magnetic electrodes with high sensitivity when the biological reactions, the material of the sensitive element, and the detection conditions are properly selected and synergistically adjusted. Figure 7 shows the magnetic field dependence of GMI ratio and the frequency dependence of maximum GMI ratio for these two cases. The most interesting feature to be noted from Fig. 7 is that the difference in GMI value for the cases with and without the ferrofluid only becomes significant at high frequencies above ~ 5 MHz, where the skin effect is dominant and the ribbon surface becomes very sensitive to magnetic signals. We note that in this frequency range, the movement of magnetic domain walls in the ribbon is strongly damped, and the magnetization process is purely caused by rotation of magnetic moments. This means that at $f > 5$ MHz, application of a DC magnetic field could align simultaneously the magnetic moments of the magnetic nanoparticles and the magnetic ribbon in the DC magnetic field direction, leading to an enhanced GMI effect. In addition, the difference in GMI is mainly observed at low magnetic fields (see inset of Fig. 7). These findings are of practical importance in selecting the optimal working conditions (magnetic field and frequency) for magnetic biosensors.

In the next stage of this project, we will use the magnetic ribbons or magnetic microwires with optimized GMI effect as the sensing elements for sensing the presence of magnetic nanoparticles on the surface of the ribbon/wire. Fe_3O_4 and CoFe_2O_4 nanoparticles of different particle size will be used to study the influence of superparamagnetic and ferromagnetic signals from nanoparticles using the surface impedance and hence the GMI effect of the ribbon.

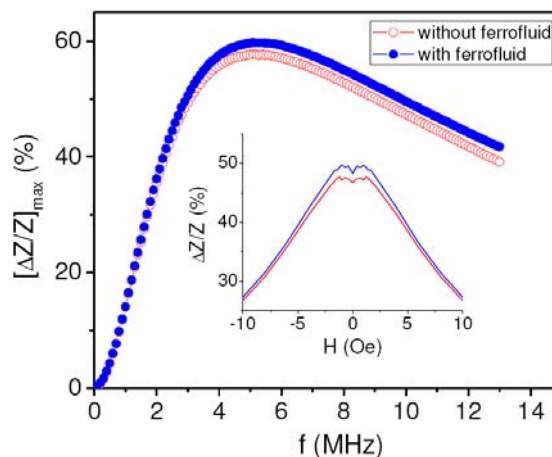


Figure 7: Frequency dependence of maximum GMI ratio and the inset shows the magnetic field dependence

Carbon nanotube based sensors

The goal of this project is to develop multifunctional materials based on carbon nanotubes for electromagnetic sensing of biological and chemical analytes in the vapor and liquid phases. In recent years, carbon nanotubes (CNTs) have been used in many potential applications including nano-devices, sensors, ultra high strength engineered fibers, quantum wires and catalyst supports [6-12]. Carbon nanotubes are attractive candidates for supercapacitors due to their high electrical conductivity and controllable mesoporosity arising from the central nanotube canal and voids formed from nanotube entanglements. Hybrid nanocomposite materials composed of carbon nanotubes loaded with nanoparticles have also been studied for supercapacitors. Recently, it has been reported that Fe_3O_4 filled CNTs may be used as diffraction gratings, optical filters and polarizers [13]. Other applications of these materials include cantilever tips in magnetic force microscopes, magnetic stirrers or magnetic valves in nanofluidic devices [13]. Since the biocompatibility of magnetite and CNTs are somewhat well-established in the literature [14,15], the combination of these two nanostructured elements could be of potential interest for improved drug delivery systems. Korneva *et al* proposed that these magnetically filled CNTs can potentially be used as nanosubmarines driven through blood vessels by an external magnetic field to transport drugs to specific locations in the body, as well as for medical diagnosis without surgical interference [16]. To realize such applications, it is technologically important to retain the desirable magnetic properties of magnetic nanoparticles in CNTs through control over the particle size and uniformity of packed particles. Despite a number of previous studies, filling CNTs completely with monodisperse Fe_3O_4 nanoparticles has remained a challenging task. Moreover, it is essential to understand the magnetic interactions that are likely to influence the magnetic properties of Fe_3O_4 -filled CNTs. In the second year of the project, we perfected the synthesis and evaluated the structural and

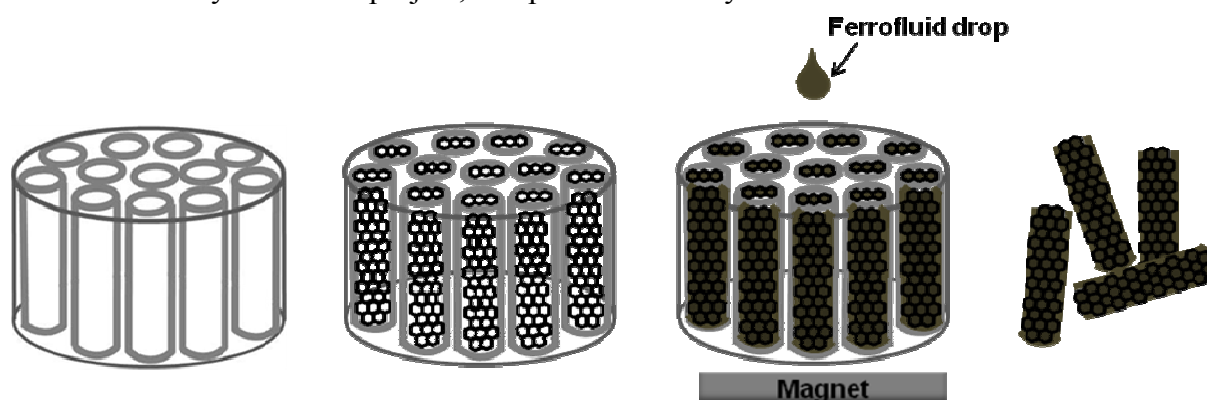


Figure 8: Scheme of the synthesis steps: (i) Alumina template, (ii) CNT grown by CVD technique inside the template, (iii) CNTs filled by ferrofluids dropwise keeping a magnet underneath the template, (iv) CNTs filled with ferrofluid after removing the template.

magnetic properties of hollow, straw-like CNTs (open at both ends) filled with Fe_3O_4 nanoparticles. A manuscript based on the work done has been accepted in the journal *Nanotechnology* and is scheduled to appear in Fall 2009.

A facile, multi-step process is utilized to fabricate these structures. First, we synthesized the magnetite nanoparticles chemically and separately used chemical vapor deposition (CVD) to grow multi-walled CNTs within the pores of alumina templates. The Fe_3O_4 NPs were incorporated inside the CNTs using a magnetically-assisted capillary action method [16]. We

demonstrated that the optimization of loading conditions in a magnetically assisted capillary action technique allows production of CNTs filled completely with uniformly dispersed Fe_3O_4 nanoparticles. Further, the increased dipolar inter-particle interaction leads to the enhanced magnetic properties of these nanostructures. Detailed magnetic characterization was performed using DC and AC susceptibility experiments. To our knowledge this is the first report of uniformly filled CNTs displaying large saturation magnetization which would render them useful for various applications.

We briefly describe the multi-step process involved in the fabrication of magnetic nanoparticle loaded carbon nanotubes. The entire process consisted of three different steps (Figure 8): (i) synthesis of Fe_3O_4 nanoparticles; (ii) carbon nanotubes grown by CVD technique; (iii) filling of the carbon nanotubes by as-prepared Fe_3O_4 nanoparticles.

Synthesis of Fe_3O_4 nanoparticles

The nearly spherical Fe_3O_4 nanoparticles were synthesized using the procedure introduced by Sun *et al*[17]. Briefly, 2mmol Iron (III) acetylacetonate ($\text{Fe}(\text{acac})_3$), 10 mmol 1,2-hexadecanediol, 6 mmol oleic acid, 6 mmol oleylamine, and 20 ml benzyl ether were mixed together and magnetically stirred under the flow of argon at 200°C for 2 h. Then the mixture was heated to reflux at 300°C for 1 h. The black colored material was cooled down to room temperature. 40 ml ethanol was added to the mixture and the precipitate was separated by centrifugation. The product was dissolved in hexane in the presence of oleic acid and oleylamine. This solution was centrifuged to remove the undispersed residue. The product was precipitated again with ethanol and centrifuged to remove the solvent and finally dissolved in hexane for further characterization.

Synthesis of carbon nanotubes

Carbon nanotubes were produced using a chemical vapour deposition (CVD) method and directly grown inside the pores of alumina membranes. The procedure was similar to that reported by Miller *et al* [18]. Before the growth of CNTs, the alumina template membranes were placed between two quartz slides and heated to 740°C for 1h to prevent the bending of templates during the CNT synthesis. The heat – treated alumina template membrane (13 mm diameter, $60\mu\text{m}$ thick and $0.2\ \mu\text{m}$ pore size purchased from Whatman) was placed vertically inside the quartz tube. The quartz tube loaded with the alumina template was placed inside the CVD reactor furnace and its temperature was increased to 670°C under the flow of argon (flow rate 20 sccm). When the temperature stabilized at 670°C , the gas flow was switched to 30% ethylene and 70% helium at a flow rate of 20 sccm. The reaction was continued for 6 h and the gas flow was switched back to argon at the flow rate of 20 sccm. The furnace was turned off and allowed to cool down to room temperature still maintaining the flow of argon. Note that while attempts were made to use alumina with smaller pore size as quoted by the manufacturers, the nanotubes grown were on average much larger (in the 250 to 300 nm range). This is most likely due to non-uniformity of the pore size through the depth of the $60\ \mu\text{m}$ thick alumina templates.

Filling the CNTs with Fe_3O_4 nanoparticles

The next step was filling the carbon nanotubes (open at both ends) encased in the alumina templates with the organic solvent containing the suspended Fe_3O_4 nanoparticles. Before filling the nanotubes, a permanent magnet ($\mu_0H = 0.4\ \text{T}$) was placed underneath the template and the hexane solution of Fe_3O_4 was poured dropwise on the top end of the template. The ferrofluid

invaded the pores due to capillary action and the homogeneous magnetic field helped to increase the rate and depth of penetration. After the evaporation of hexane at room temperature, the template was broken into tiny pieces and dipped into 4.0 M NaOH solution and sonicated till the template dissolved completely. After sonication, the solution was vacuum filtered through a polyester nucleopore membrane (pore size $\sim 0.2 \mu\text{m}$). After filtration, the residue was rinsed with toluene to remove the stray ferrofluid particles from the surface of the membrane. Then the residue was washed with isopropanol and deionized water for several times and finally dried at room temperature. The dry sample was collected for structural characterization and magnetic measurements.

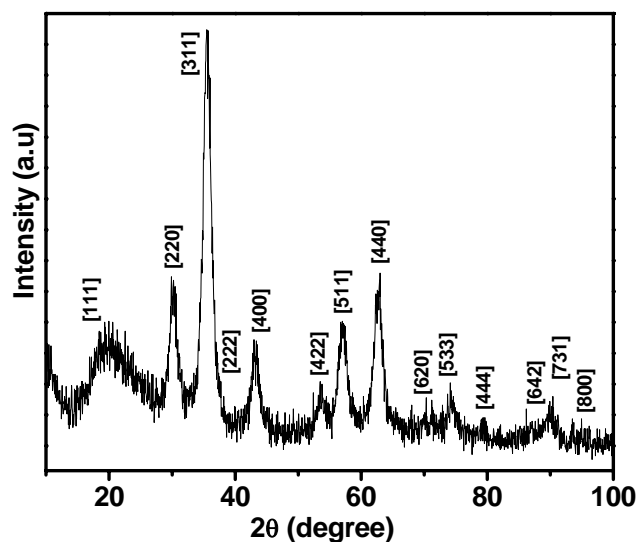


Figure 9: XRD pattern of Fe_3O_4 nanoparticles

Structural Characterization

The inverse spinel crystal structure of magnetite was confirmed by X-ray powder diffraction (Fig 9) using a Phillips diffractometer with a $\text{CuK}\alpha$ source. The size and shape of iron oxide nanoparticles and the nanoparticle filled CNTs were characterized using a Morgagni transmission electron microscope (TEM). For TEM characterization, the iron oxide nanoparticles

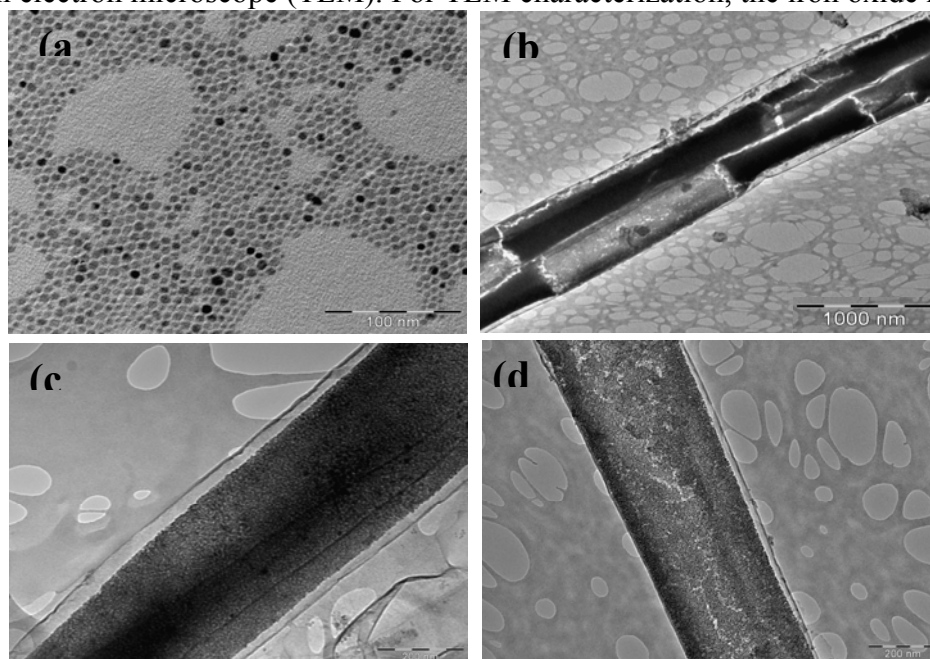


Figure 10: TEM micrographs of (a) Fe_3O_4 nanoparticles and (b,c,d) carbon nanotubes filled with Fe_3O_4 nanoparticles.

suspended in hexane and iron oxide loaded CNTs suspended in isopropanol were drop cast on a carbon-coated Cu grid. The average particle size of Fe_3O_4 was estimated from a histogram analysis to be 6 ± 0.5 nm (Figure 10a). Several different views of the nanoparticle loaded CNTs are shown in Figure 10((b), (c), (d)). It can be seen that the particle packing within the cross-section of the nanotubes is very uniform. The average length of CNT is 5-6 μm and diameter is 250-300 nm with 30 nm wall thickness. So the aspect ratio of these magnetic nanotubes turns out to be ~ 20 .

Magnetic characterization

Standard magnetic measurements such as temperature dependence of zero-field-cooled

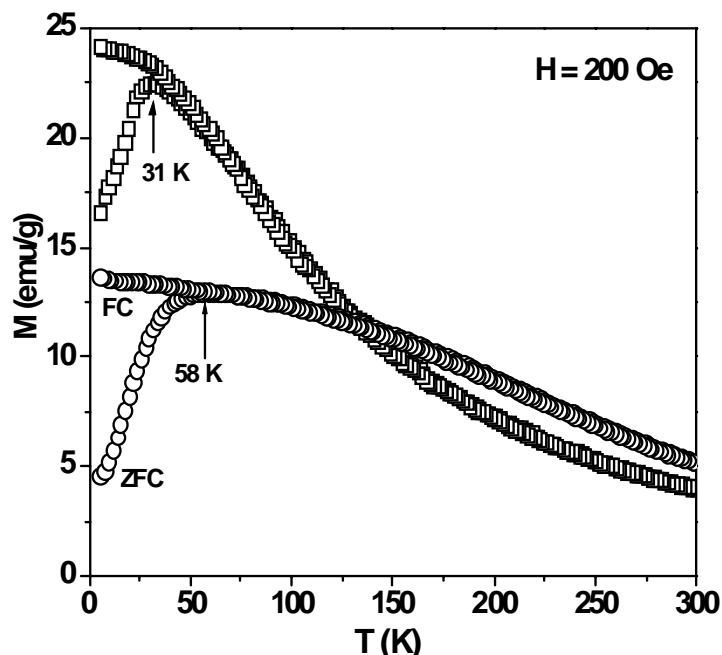


Figure 11: M vs T plot of Fe_3O_4 nanoparticles (\square) and carbon nanotubes filled with Fe_3O_4 nanoparticles (\circ).

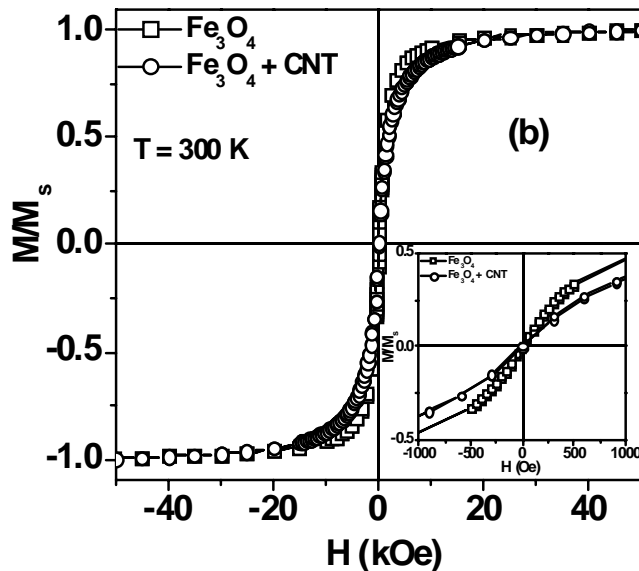


Figure 12: M vs H plot of Fe_3O_4 nanoparticles (\square) and carbon nanotubes filled with Fe_3O_4 nanoparticles (\circ) at 300 K. ($M_s = 60$ emu/g for Fe_3O_4 NPs and 63 emu/g for carbon nanotubes filled Fe_3O_4 NPs)

(ZFC) and field-cooled (FC) susceptibility, M-H hysteresis loop measurements, and AC susceptibility were done using a commercial Physical Property Measurement System (PPMS) from Quantum Design over a wide range of temperature and magnetic fields. Figure 11 shows the zero-field-cooled (ZFC) and field-cooled (FC) DC magnetization curves for Fe_3O_4 NPs and CNTs filled with Fe_3O_4 NPs (labeled as Fe_3O_4 -CNTs) taken at a field of 200 Oe. The ZFC curve for Fe_3O_4 NPs exhibits the typical blocking process of an assembly of super-paramagnetic particles with a distribution in blocking temperature around an average $T_B \sim 31$ K. However, the case is quite different for Fe_3O_4 -CNTs, which exhibit a broad ZFC curve with its peak at ~ 58 K. For this sample, the gradual

decrease in magnetization above 58 K, deviating from Curie type $1/T$ dependence, is characteristic of the presence of particle interactions in this system [19].

Figure 12 and its inset shows the magnetic field dependence of magnetization (the M-H curves) taken at 300 K. It can be observed that for both Fe_3O_4 NPs and Fe_3O_4 -CNTs the M-H curves at 300 K do not show any hysteresis, consistent with superparamagnetic behavior. At 5 K the values of saturation magnetization (M_s) of Fe_3O_4 NPs and Fe_3O_4 -CNTs are determined to be about 60 emu/g and 63 emu/g, respectively. Likodimos *et al* [20] have shown that pure CNTs exhibit a diamagnetic behavior with $M = -0.7$ emu/g at an applied field of 50 kOe. Subtracting the diamagnetic contribution of CNTs, the M_s of Fe_3O_4 -CNTs is ~ 63.7 emu/g. This value is smaller than that of bulk Fe_3O_4 ($M_s \sim 92$ emu/g) but is larger compared with that of Fe_3O_4 NPs ($M_s \sim 60$ emu/g). The enhancement of M_s for Fe_3O_4 -CNTs is very important from the point of view of magnetic-field guided applications. The slight enhancement of the magnetization in Fe_3O_4 -CNT system in comparison with the as-synthesized Fe_3O_4 nanoparticles is also consistent with enhanced inter-particle interactions (due to tight packing of the particles within the confined region of the hollow nanotubes) that is discussed and quantitatively analyzed in our 2009 publication in Nanotechnology [21].

Functional materials for affecting cell proliferation and locomotion

In this project, we are looking at several nanoscale structures where the basic functionality such as magnetic and metallic properties can be used for biomedical diagnostics and cell manipulation. We have synthesized water-soluble, biocompatible nanoparticles and conducted studies on cell uptake using optical microscopy and electric cell substrate impedance sensing (ECIS).

Superparamagnetic iron oxide nanoparticles have drawn special attention for various biomedical applications such as diagnosis, therapeutics, separations, contrast agent for magnetic resonance imaging [22-24]. This is because they possess high saturation magnetization and are also less toxic than the other metal or metal oxide nanoparticles. In general nanoparticles suitable for biomedical applications should be (i) highly water dispersible, (ii) monodisperse (iii) surface modified by biocompatible reagents. In this work we have synthesized highly water dispersible polyethylene glycol (PEG) diacid surface-modified iron oxide nanoparticles.

We have synthesized Fe_3O_4 nanoparticles and functionalized them with polyethylene glycol (PEG). PEG is an amphiphilic polymer and coating on Fe_3O_4 by PEG makes iron oxide particles biocompatible. The synthesis procedure is outlined below:

Synthesis of Fe_3O_4 nanoparticles

The synthesis and surface functionalization of Fe_3O_4 nanoparticles followed the procedure described by Sun *et al* [24]. Briefly 2 mmol of iron (III) acetylacetonate [$\text{Fe}(\text{acac})_3$], 10 ml benzyl ether and 10 ml oleylamine were mixed together. The solution was heated to 110°C for 1h and finally to 300°C for 2h. The solution was cooled to room temperature and 50 ml ethanol was added to it. The black precipitate was collected by centrifugation and this procedure was repeated three times. Finally the product was redispersed in hexane and 0.25 ml of oleic acid was added to stabilize the particles.

Surface functionalization of Fe₃O₄ nanoparticles

PEG diacid (20 mg), 2 mg N-hydroxysuccinimide, 3 mg N, N' dicyclohexylcarbodiimide and 1.27 mg dopamine hydrochloride were dissolved in a solvent mixture of 2 ml chloroform and 1 ml dimethyl formamide. Anhydrous Na₂CO₃ (10 mg) was added to the reaction mixture. Then the reaction mixture was stirred at room temperature for 2h. 5 mg Fe₃O₄ nanoparticles were added and the reaction mixture was stirred overnight in presence of argon at room temperature. The modified Fe₃O₄ nanoparticles were precipitated by adding hexane. The precipitate was collected by a

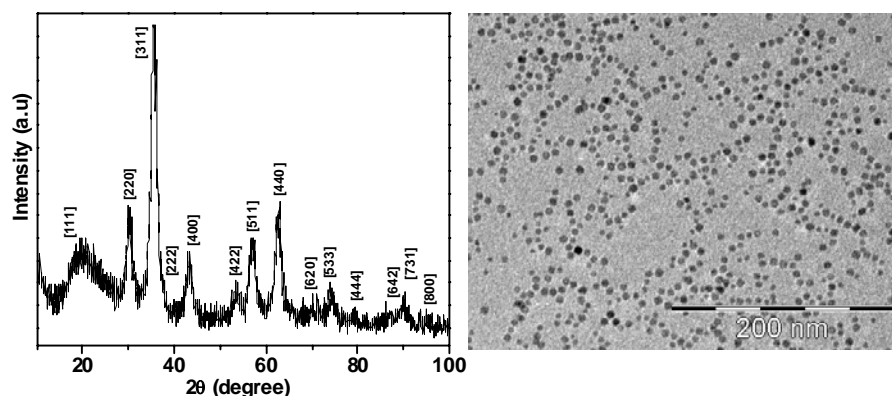


Figure 13: Structural characterization (XRD and TEM) of water-soluble, biocompatible nanoparticles

permanent magnet and dried under Ar. The particles were dispersed in water. Figure 13 shows the XRD and TEM characterization of these nanoparticles. XRD shows pure Fe₃O₄ phases present in the sample and TEM image shows that the particles are nicely dispersed in water without any agglomeration. The particle size is 4-5 nm.

Cell culture

The 3T3 cells and the water dispersed Fe₃O₄ nanoparticle-loaded 3T3 cells were incubated at 37 °C (5% CO₂) overnight. Three different concentrations (10, 100 and 300μl) of nanoparticles were added to a certain number of cells. The nanoparticles uptake by cells was studied by optical microscopy and electric cell substrate impedance sensing (ECIS) measurement (Fig. 14).

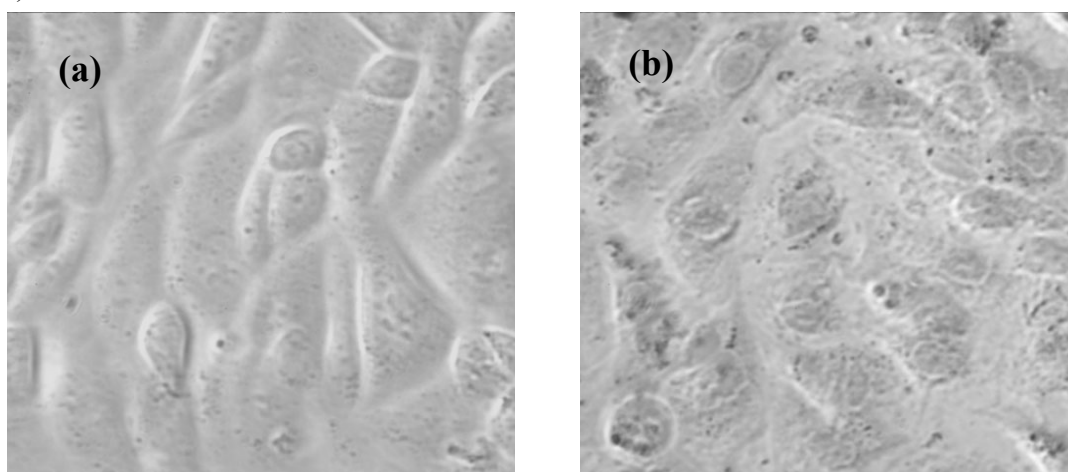


Figure 14: Optical microscopy image of (a) 3T3 cells as control/medium and (b) Fe₃O₄ nps labeled 3T3 cells.

Optical microscopy study

The microscopic images show the intercellular dispersion of the particles and that no adverse effect has been observed upon nanoparticle labeling in cells.

Electric cell substrate impedance sensing (ECIS) measurement

In this measurement we have studied the resistance with time for all samples including the control (see Figure 15). Electrode arrays, relay bank, lock-in amplifier and software for the ECIS measurement and data analysis were from the instrument commercialized by Applied

BioPhysics (Troy, NY).

Each electrode array consisted of eight wells which was 1 cm in height and 0.8cm² in bottom area; each well contained a 250μm diameter gold electrode (area $\sim 5 \times 10^{-4}$ cm²) and a much larger gold counter electrode. The large electrode and one of the small electrodes were connected via the relay bank to a phase-sensitive lock-in amplifier. A 1V AC signal at 4 kHz was

applied to the sample through a 1MΩ resistor to maintain an approximately constant current of 1μA through the sample i.e. the in-phase voltage was proportional to the resistance, and the out-of-phase voltage was proportional to the capacitive reactance. For impedance measurement of 3T3 cells upon addition of Fe₃O₄ particles, the samples were cultured for 24 h.

The time-series data were normalized and numerically analyzed by calculating power spectrum and variance (the square of the standard deviation). The normalized resistance with time plot and variance with time plot of the nanoparticle-loaded samples are similar to the control sample which indicate that the cell viability is not affected by the nanoparticle loading upto 300μl concentration of nanoparticles. Further studies and analysis are under way and will be reported in the next annual report.

Conclusions: We have prepared highly water dispersible iron oxide nanoparticles. Optical microscopy images and the ECIS data clearly show the particles' uptake by the 3T3 cells and ECIS data shows that the cells containing the Fe₃O₄ nanoparticles can survive for 24h without cell death.

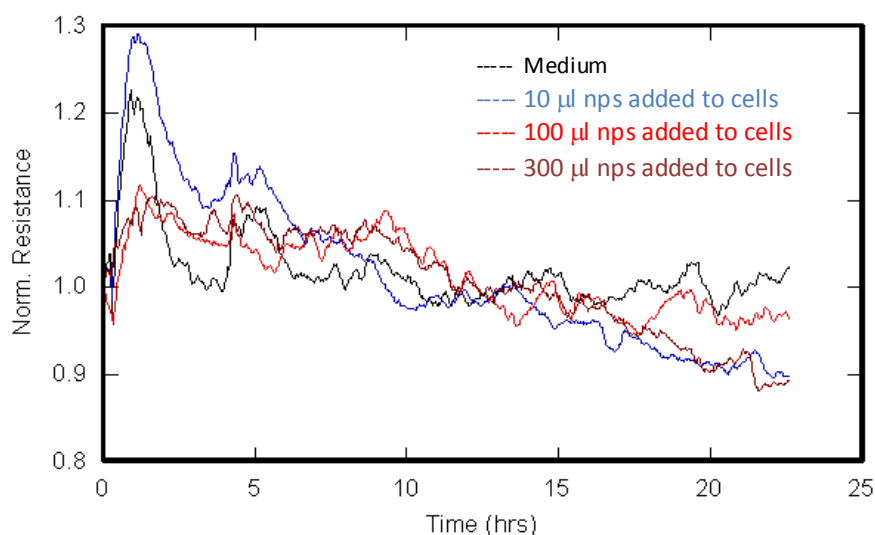


Figure 15: ECIS spectra of cells loaded with different concentrations of biocompatible nanoparticles

Task II: Multifunctional composites for communication and energy applications

Tunable multifunctional nano- and heterostructures for RF and microwave applications

Multiferroic bilayers of Cobalt Ferrite and PZT:

The objective of this project is to fabricate bilayers of ferroelectric $\text{Pb}(\text{Zr}_{1-x}\text{Ti}_x)\text{O}_3$ [$x=0.48$] (PZT) and ferromagnetic CoFe_2O_4 (CFO) epitaxially and to investigate the multiferroic coupling between the layers. The coupling of the electric polarization in PZT and the magnetic moment in CFO is mediated by the film interfacial stress. Development of such multifunctional materials will enable the fabrication of ultra sensitive sensors for biological cells and agents. In the 1st and the 2nd quarters of the second year of this project we reported initial results of interfacial stress investigated by x-ray diffraction techniques. In the 3rd and 4th quarter we continued this analysis and the combined results are presented below.

Crystal Structure Analysis

We have grown thin films of CFO epitaxially on MgO (100) and STO (100) substrates by pulsed laser ablation. The film crystallinity and the orientation were assessed by conventional θ - 2θ x-ray diffraction (XRD) methods. Quantification of film-substrate and inter-film stress in single film and heterostructures is important as the magnetoelectric coupling results from stress mediation. The stress on the film was measured using a $\sin^2\psi$ technique. Fig. 16 shows the XRD peaks for the powder target and for the films grown on MgO and STO substrates. The peaks that correspond to cobalt ferrite face-centered cubic lattice belong to the space group $Fd\bar{3}m$ (227). The films grown on MgO (100) and STO (100) show peaks corresponding only to (400) peak of CFO indicating high degree of alignment. The insets in Fig. 16b and Fig. 16c show the (400) rocking curve diffraction patterns of the lattice matched CFO. The full width at half maximum (FWHM) of this peak for MgO is 0.076° , showing excellent crystallographic orientation along the (L00) direction that is indicative of high degree of epitaxy. FWHM of the rocking curve patterns of films grown on STO is 0.915° due to the large lattice mismatch with CFO. Since (200) of MgO and (400) of CFO diffraction peaks are very close to each other, Φ scan measurements were conducted using Bragg's reflection from the (311) plane of cobalt ferrite. The peaks of the Φ spectra occur at intervals of 90° , confirming the cubic symmetry and epitaxial growth. Because of larger lattice mismatch, (400) peak of CFO is shifted significantly in films that were grown on STO (Fig. 16b). Inset in Fig. 1b also shows the Φ scan curves from (311) reflection of cobalt ferrite films that were deposited on STO substrates. Energy dispersive spectroscopy (EDS) was used to confirm the stoichiometry of the films.

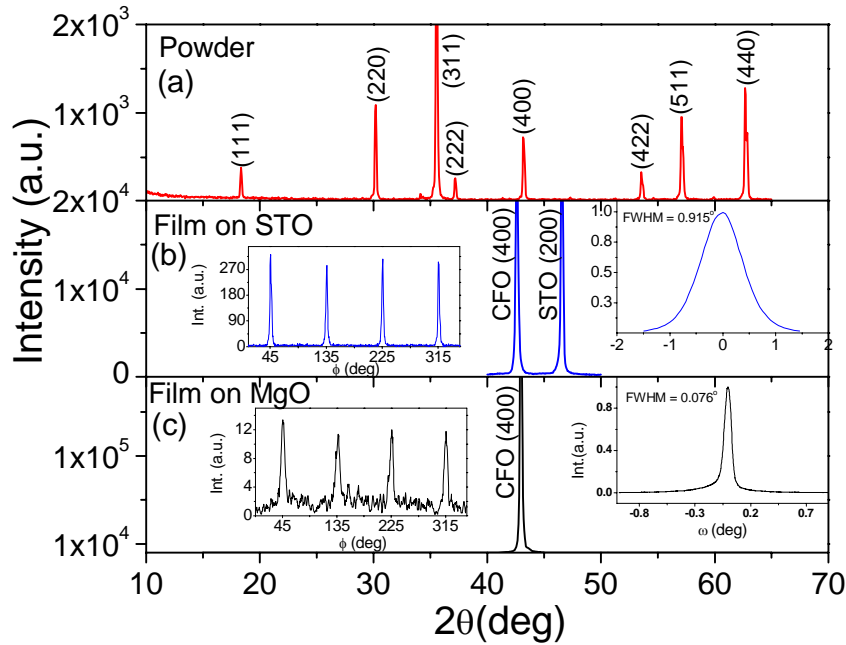


Figure 16: (a) XRD peaks of powder target of cobalt ferrite. (b) XRD peak of epitaxial 200 nm thick film of cobalt ferrite (CFO) grown on STO (100) substrate. The left peak is from CFO (400) which is shifted toward the left due to large lattice mismatch with substrate. The right peak is from the substrate. The left inset shows Φ scan spectra from (311) reflection. The right inset shows rocking curve of (400) peak with FWHM of 0.915° . (c) XRD peak of epitaxial 200 nm thick film of cobalt ferrite (CFO) grown on MgO (100) substrate. The (400) peak of CFO overlaps with the (200) peak of MgO. The left inset shows Φ scan spectra from (311) reflection. The right inset shows rocking curve of (400) peak with FWHM of 0.076° .

Magnetic anisotropy in CFO thin films

Magnetic measurements were conducted for in-plane and out-of-plane configurations of the films in magnetic fields up to 50 kOe. Figure 17 shows the M-H loops measured at 300K and at 10K for epitaxial thin films of the same thickness (200 nm). The easy axis of magnetization of the films grown on MgO was observed to be out of the plane of the film along the [100] direction, whereas the films grown on STO have the easy axis of magnetization along the plane of the film. This contrasting difference in magnetic anisotropy for these two films can arise from the fact that the CFO films (lattice constant=8.39 Å) grow with tensile strain on MgO (2 x lattice parameter=8.42 Å) while films grown on STO (2 x lattice parameter=7.81 Å) substrates undergo compression. In particular, the stress present due to the mismatch between the film and the substrate may have played a significant role in the observed anisotropy.

We have calculated the uniaxial anisotropy by using the difference between the in-plane and out-of-plane magnetization obtained from Fig. 17. The uniaxial magnetic anisotropy is given by [25]

$$K_u = \int_0^{M_s} (H_{eff}^{out} - H_{eff}^{in}) dM \quad (1)$$

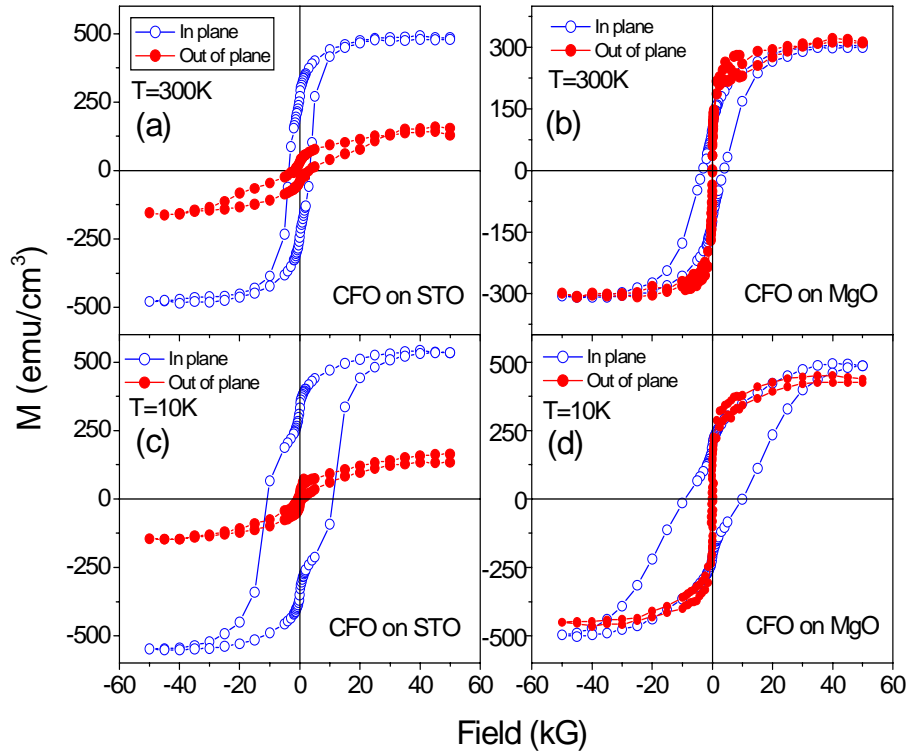


Figure 17: (a) and (c) M-H loops measured at 300K and 10 K respectively of the 200 nm thin film grown on STO (100) for in plane and out of plane configuration. (b) and (d) M-H loops measured at 300K and 10 K respectively of the 200 nm thin film grown on MgO (100) for in plane and out of plane configuration.

where $H_{eff} = H_{ex} - NM$, N = demagnetization factor, M = magnetization, H_{ex} is the external field applied and M_s is the saturation magnetization. The superscripts *out* and *in* refer to the out-of-plane and in-plane orientation of the films with respect to the applied magnetic field. For the case of a thin film with uniform magnetization in all x, y and z direction, equation (1) reduces to

$$K_u = H_{ex}^{out} M_s^{out} - H_{ex}^{in} M_s^{in} - \frac{1}{2} (M_s^{out})^2 \quad (2)$$

The uniaxial magnetic anisotropy calculated for films grown on MgO substrates is $K_u = 9.44 \times 10^6 \text{ erg/cm}^3$. This value of K_u is three-fold larger than the intrinsic magnetocrystalline anisotropy of bulk cobalt ferrite ($3 \times 10^6 \text{ erg/cm}^3$) [26,27]. This indicates that the large anisotropy seen in the film grown on MgO likely arises from the interfacial stress resulting from the lattice mismatch between the film and the substrate.

For the case of the films grown on STO (100), the out-of-plane magnetization is not saturated up to an applied field of 50 kOe (see Fig. 17). Therefore, it is not precise to use Eq. (2) to estimate the magnetic anisotropy for this film. Alternatively, we have estimated the magnetic anisotropy of this film by using the difference between the lattice parameter of bulk cobalt ferrite (8.39 Å) and the corresponding thin film (8.28 Å). This large change in the thin film value is caused by the large mismatch between the lattice parameter of cobalt ferrite and the STO

substrate ($2 \times 3.905 = 7.81 \text{ \AA}$). The strain (ϵ) due to the difference between the bulk and film lattice constants is 0.013. Thus the stress $\sigma = Y \epsilon$ (Young's modulus [28] $Y_{100} = 1.5 \times 10^{12} \text{ dyne/cm}^2$) is $19.67 \times 10^9 \text{ dyne/cm}^2$. Magnetoelastic stress anisotropy constant can be estimated by $K_a = (3/2) \lambda_{100} \sigma$, where λ_{100} for CFO [27,28] is -590×10^{-6} . Calculated value of V is $17.4 \times 10^6 \text{ erg/cm}^3$. This value is larger compared to that obtained for the films grown on MgO (100). This is consistent with the fact that stress is larger for the films grown on STO than for the films grown on MgO. It is the presence of larger stress in the film grown on STO that causes a larger shift in the (400) Bragg reflection compared to the bulk (Fig.16a and Fig. 16b). The anisotropy field (H_a) of the films grown on STO computed using the expression $H_a = 2K_a/M_s$ is estimated to be about 72.5 kOe.

Stress measurement ($\text{Sin}^2\psi$ technique)

To provide further insight into the importance of stress in the observed magnetic anisotropy in the CFO thin films, we have used the $\text{sin}^2\psi$ technique (the direct stress measurement technique) to evaluate the stress and relate these measurements to the anisotropy of the films grown on MgO. The $\text{sin}^2\psi$ technique is a standard non-destructive technique to measure residual stress in a material. In this technique a textured film is scanned in the vicinity of the Bragg reflection (2θ). A shift in the Bragg reflection (2θ) is observed if a strained film is tilted by an angle (ψ). The scanning configuration is shown in the lower inset of Fig.18. The shift in 2θ is used to calculate the new value of interplanar spacing (d). It has been found that d is linearly varied as a function of $\text{sin}^2\psi$ as shown below[29].

$$d_\psi = \left(\frac{1+\nu}{Y} \right) d_o \sigma \text{sin}^2 \psi - \frac{\nu}{Y} (\sigma_{11} + \sigma_{22}) d_o + d_o \quad (3)$$

The slope of d_ψ vs. $\text{sin}^2\psi$ plot is used to compute the value of the stress σ if the Poisson's ratio (ν) and the Young's modulus (Y) of the particular material are known. The unstrained interplanar distance d_o can be replaced with the value of d when the tilt angle is zero. It should be noted here that the above relation is modified for $\varphi=0$.

Figure 18 shows the 2θ scans of CFO-MgO film for various ψ tilts. The values of d were calculated using the shift in the Bragg reflection for different tilt (ψ) angles. The different values of d are plotted as a function of $\text{sin}^2\psi$ (upper inset of Fig.18). Fairly linear fit was observed indicating that the residual stress within the area under scan was nearly homogeneous. The slope of the fit obtained provides a qualitative measurement of the residual stress in the thin films. By using the slope of the fit and equating that to the coefficient of $\text{sin}^2\psi$ term in Eq. (3) we have calculated the stress (σ) for CFO-MgO to be $\sigma = -12.2 \times 10^9 \text{ dyne/cm}^2$. The values of Y , ν and d_o for CFO are: $Y = 1.5 \times 10^{12} \text{ dyne/cm}^2$, $\nu = 0.26$ [30] and $d_o = 2.1039 \text{ nm}$. Accordingly, the stress anisotropy (K_a) is obtained from $K_a = (3/2) \lambda_{100} \sigma$, where λ_{100} for CFO is -590×10^{-6} and $\sigma = -12.2 \times 10^9 \text{ dyne/cm}^2$, to be $10.76 \times 10^6 \text{ erg/cm}^3$. This value of anisotropy is very close to that calculated from the M-H data using Eq. (2) ($K_a=9.44 \times 10^6 \text{ erg/cm}^3$). The agreement between the values obtained by these two independent methods clearly indicates that stress plays a dominant role in the observed anisotropy in the CFO thin films grown on lattice mismatched substrates. The anisotropy field (H_a) of the films grown on MgO is determined to be about 65 kOe, which is lower compared to that of the film grown on STO ($H_a=72.5 \text{ kOe}$).

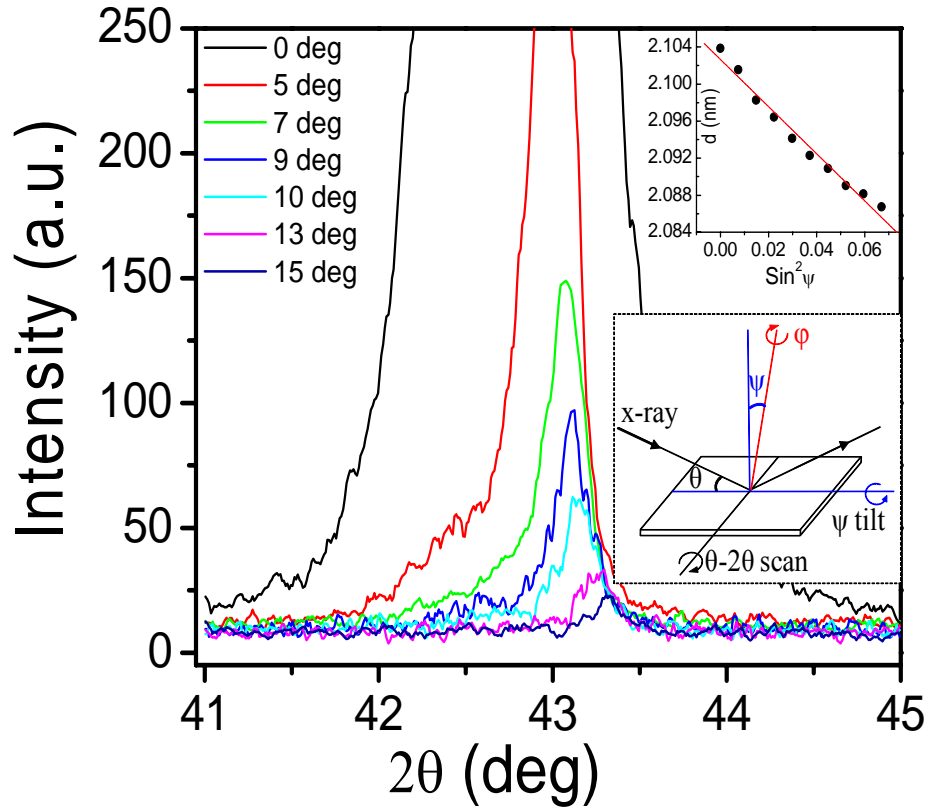


Figure 18: θ - 2θ scan about $2\theta = 43.006^\circ$ by varying the ψ angle from 0 to 15° keeping the Φ at 0° on the CFO films on MgO (100) substrate. The legend shows the values of $\sin^2\psi$. The upper inset shows the plot of d vs. $\sin^2\psi$ and a linear fit to the data points. Schematic for $\sin^2\psi$ technique is shown in the lower inset.

Detection of switching fields by Tunnel diode Oscillator (TDO) technique

While the low-field switching feature is clearly observed in the M-H loops (Fig. 17), it is difficult to determine precisely the magnetic switching field and particularly its dependence on measuring temperature. In this work, we have used a very sensitive and precise RF transverse susceptibility (TS) technique developed by Srikanth [31] et al. to probe magnetic switching and its temperature dependence in both the film grown on STO and the film grown on MgO. The RF transverse susceptibility, which is based on a sensitive, self-resonant tunnel diode oscillator (TDO), has been validated over the years to be an excellent technique for probing effective magnetic anisotropy in a wide range of magnetic materials ranging from thin films[32], nanoparticles [33] to single crystals [34]. In TS experiments, a small perturbing ac or rf field (< 10 Oe) is applied to the sample in addition to the swept dc magnetic field. Since the sample is placed in an inductive RF coil that is part of a self-resonant circuit, the shift in the resonant frequency with varying dc magnetic field and/or temperature give a direct measure of the change in inductance and hence the sample susceptibility. The change in transverse susceptibility with dc magnetic field has been expressed by

$$\left(\frac{\Delta\chi_T}{\chi_T}\right)\% = \left[\frac{\chi(H) - \chi(H_{\max})}{\chi(H_{\max})}\right] \times 100\% \quad (5)$$

where H_{\max} is the maximum applied dc magnetic field.

Theoretically, the transverse susceptibility spectrum in a unipolar field scan from positive to negative saturation should consist of three singularities of which two occur at the anisotropy fields ($\pm H_k$) and one at the switching field ($\pm H_s$)[35,36]. However, it has been experimentally shown that depending upon the magnetic nature of the sample and the orientation in which the sample is introduced in the inductive coil, either anisotropy peaks or switching peaks could be prominently observed. In the present study, RF transverse susceptibility measurements were conducted at different temperatures ($T = 300\text{K}$, 200K and 10K) for the cobalt ferrite films grown on both MgO and STO. The maximum dc field applied was 5 kOe. The results are displayed in Fig. 19 and its inset. It can be clearly seen from this figure that the TS curves show only the switching peaks. The absence of anisotropy peaks can be understood due to the fact that the

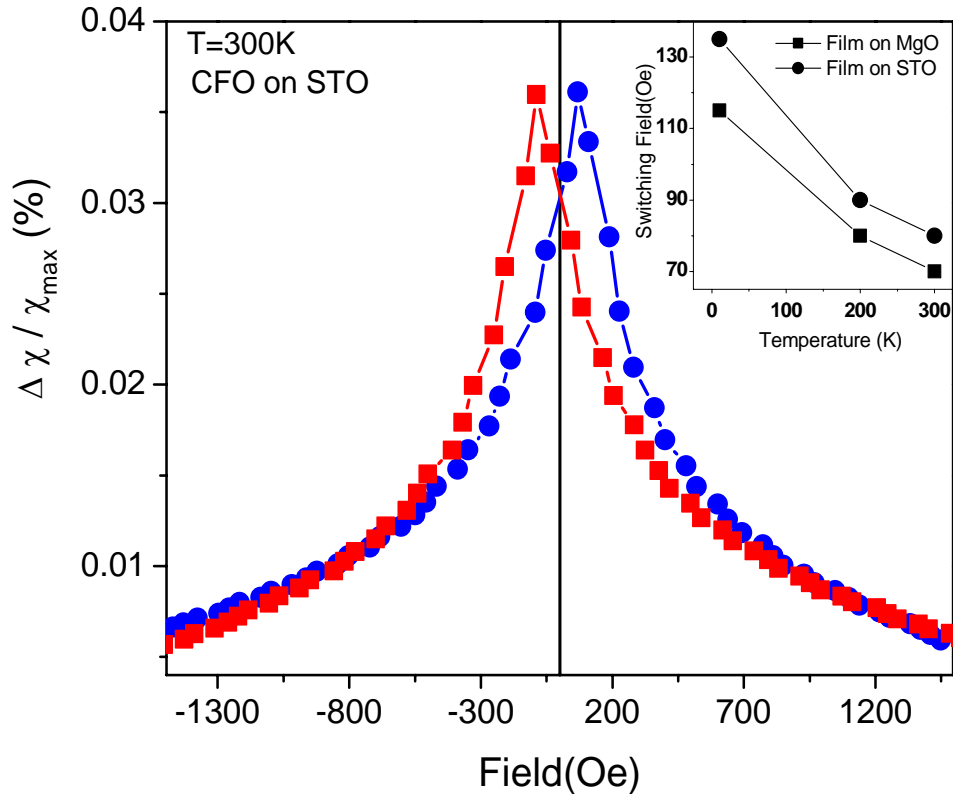


Figure 19: TDO measurement of CFO films on STO at 300K with the film plane perpendicular to the DC field. The line with solid squares represents the field sweep from positive to negative, whereas the solid circles represent the field sweep from negative to positive.

anisotropy fields of the films investigated were beyond the maximum applied dc magnetic field. However, it was possible to detect the low field switching present in the cobalt ferrite films. The change of TS peak position with temperature (see inset of Fig. 19) clearly reveals that for the

cobalt ferrite films investigated, the switching field increases as the temperature is decreased. For the films grown on MgO, the switching fields at 300K, 200K and 10 K were ± 70 Oe, ± 80 Oe and ± 115 Oe, respectively. In case of the films grown on STO, the switching fields obtained for 300K, 200K and 10K were ± 80 Oe, ± 90 Oe and ± 135 Oe, respectively. The larger values of switching field for the case of the film grown on STO may be reconciled with the fact that the lattice mismatch and thus the stress is larger in this sample. The stress due to lattice mismatch would be more significant at the interface. This indicates that the origin of the steps seen in the M-H loops of the cobalt ferrite films is associated with the stress at the interface between the substrate and the film, at least in the case of epitaxially grown films.

Optimization of PZT growth

Lead (Pb) deficiency is a major issue in the growth of PZT films at high temperature. Pb deficiency in films translates to defects that promote charge transport. As a result, it is difficult to obtain high electrical polarizations in Pb-deficient PZT films. We have attempted several ways to compensate for Pb deficiency in our films. Multiple layers of PbTiO_3 (90% excess Pb) and PZT as well as multiple layers of PbO and PZT were used to enhance Pb content. In this work Pb content of the films was significantly improved. However, the X-ray diffraction spectra of these multilayers showed impurity phases. When a PZT target of 30 % excess Pb was used the films grown on STO (100) showed excellent crystallinity, however with a lower lead content in the film (Fig. 20). The films were grown epitaxially along the (002) plane of PZT. The FWHM of the rocking-curve about PZT (100) is found to be around 0.122° (Fig. 21). Similar value was obtained for the rocking-curve about PZT (200). The measurements of electric polarization in these films are under way, and will be presented in the next report. The surface

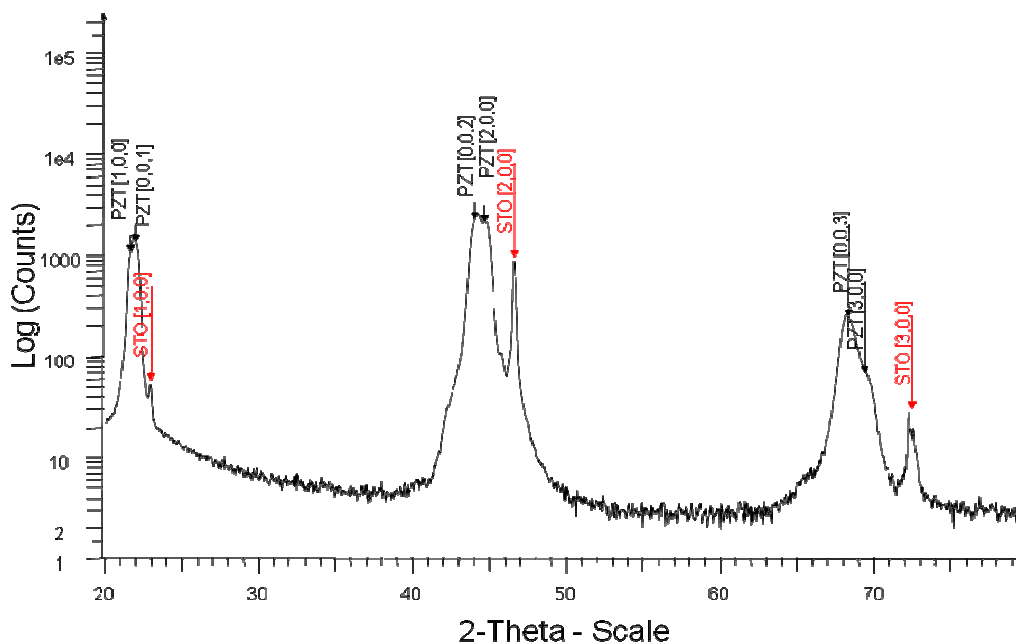


Figure 20: XRD pattern of PZT film on STO substrate from (30% excess Pb) PZT target.

of the PZT films grown on STO substrates from the target with 30% excess Pb is very smooth with very few particulates as shown in Fig. 22.

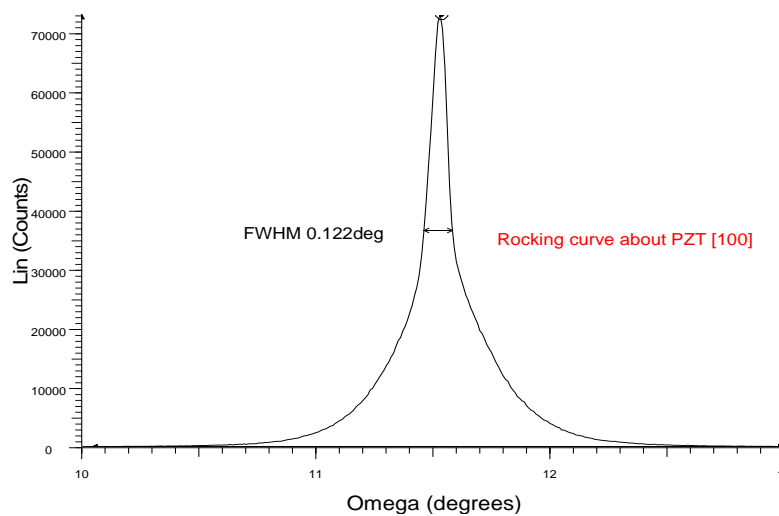


Figure 21: Rocking curve about (100) plane of the epitaxial PZT grown on STO (100)

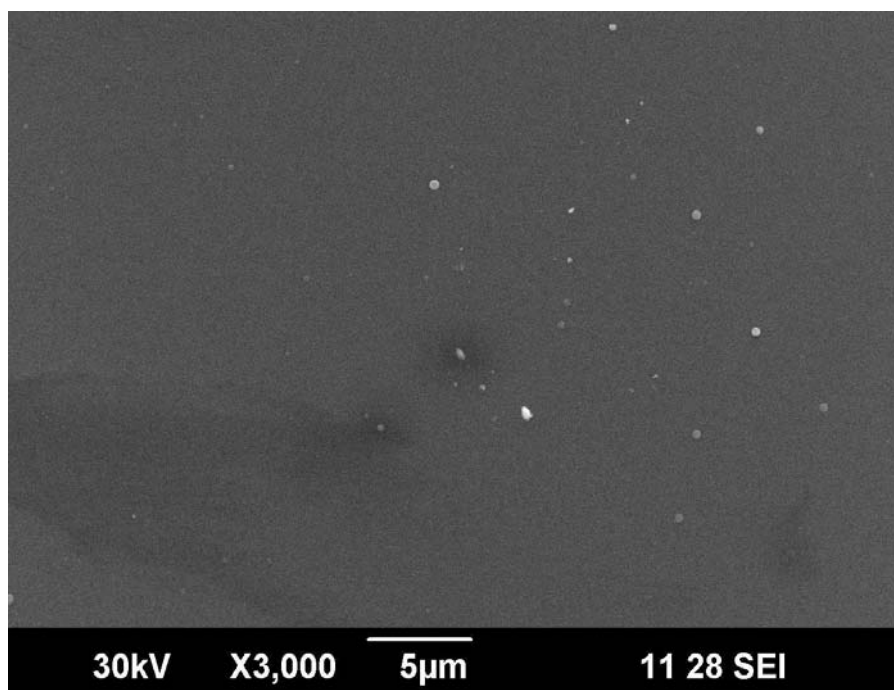


Figure 22: SEM picture of the PZT film grown on STO (100)

Ferromagnetic Mn-doped ZnO and Ferroelectric V- doped ZnO:

In previous reports we have demonstrated the existence of magnetism in Mn-doped ZnO films. In the second quarterly report we presented a possible mechanism for the manifestation of magnetism in ZnO:Mn system. The proposed RKKY interaction which comes about as a result of the interaction between charge carriers (electrons) and the magnetic ions (Mn^{2+}) in the ZnO lattice agrees well with the magnetic data obtained for 2% doped films. In the third quarter we have conducted further experiments to confirm this mechanism by studying 12% Mn-doped ZnO films.

The RKKY (Ruderman-Kittel-Kasuya-Yosida) interaction occurs when the conduction electrons in the host material interact with the magnetic moment of the doped magnetic impurity. Mn-doped ZnO is a reasonable system to apply RKKY interaction to explain the ferromagnetism observed as it has already been used to explain magnetism in the dilute alloys of Mn in Au [37]. The RKKY potential between the Mn impurities mediated by the charge carriers is given by

$$U_{RKKY}(r) = -J_{RKKY}(r) \mathbf{S}_1 \cdot \mathbf{S}_2 \quad (6)$$

where $J_{RKKY}(r) = V_0 \cos(2k_F r)/r^3$. Here k_F is the Fermi vector and r is the inter-impurity particle distance. We see that $V(r)$ is proportional to $1/r^3$ and has an oscillatory nature as shown in Fig. 23. For dilute magnetic impurities the interaction is mostly ferromagnetic. We have chosen two specific impurity concentrations. For 2 at. % Mn doping on ZnO, the inter-impurity spacing would be around 0.94 nm and for 12 at.% of Mn doping the impurity spacing would be 0.44 nm. Both these concentrations favor ferromagnetic order since $J_{RKKY}(r)$ is positive, but the 12 % doping should enhance the ferromagnetism.

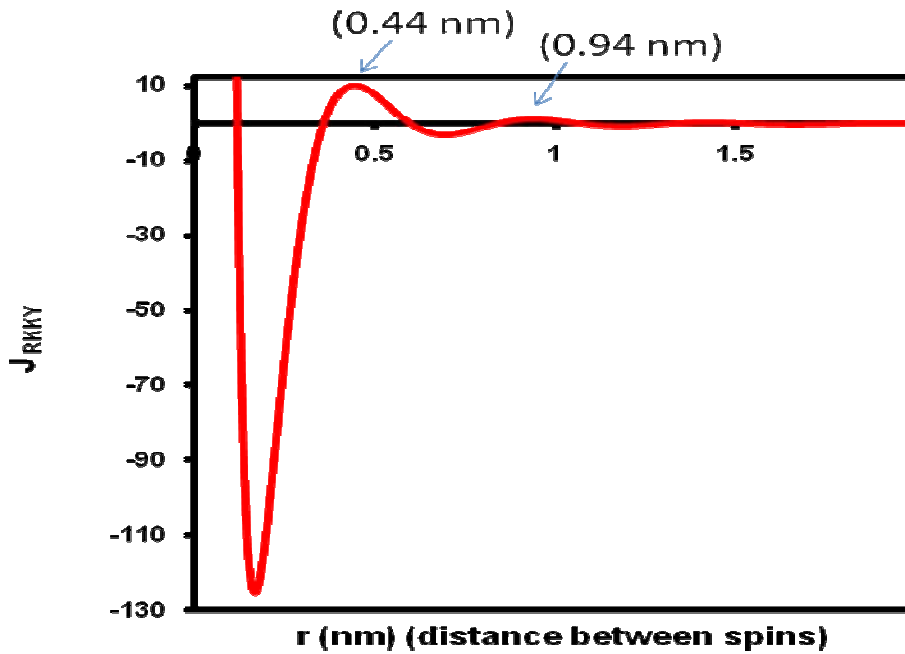


Figure 23: RKKY interaction as a function of impurity spacing

We have fitted the magnetic data using the proposed RKKY type mechanism for magnetism in these films (Fig.24). The strength of RKKY interaction V_0 can be found by comparing the saturation magnetization data using [37]:

$$M = g\mu_B S_n \left[1 - \frac{2(2s+1)nV_0}{3g\mu_B H} \right] \quad g\mu_B H \gg k_B T \text{ and } nV_0 \quad (7)$$

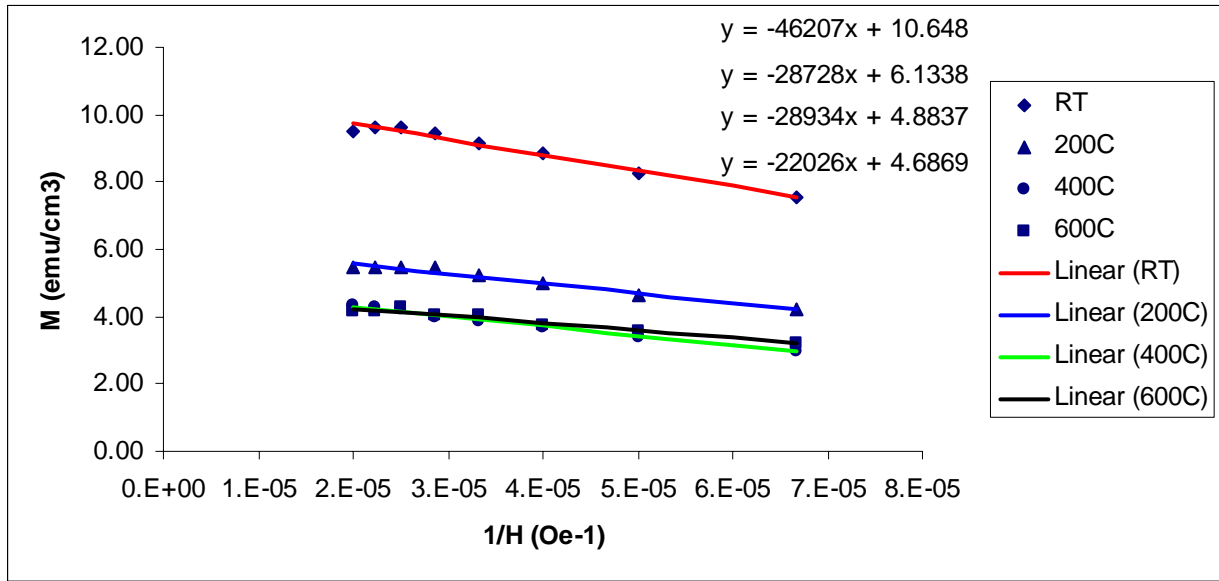


Figure 24: M vs. H^{-1} plot at 10 K for Mn doped ZnO films grown on sapphire substrate

From the slope and intercept of the above plot we have calculated n , V_0 and average Mn-Mn distance (r). The values were calculated assuming that $g=2$ and Mn^{2+} oxidation state for which $S=5/2$. The value of the RKKY strength (V_0) is comparable to the reported value ($V_0=7.5 \times 10^{-37}$ ergcm³) of the dilute CuMn alloys [37]. The calculated values are shown in the table below:

	intercept	slope	$n(\text{cm}^{-3})$	V_0 (erg cm ³)	nV_0 (eV)	r (nm)
30	10.648	46207	$2.30\text{E}+20$	$1.50\text{E}-37$	$2.16\text{E}-05$	$1.91\text{E}+00$
200	6.1338	28728	$1.32\text{E}+20$	$2.81\text{E}-37$	$2.33\text{E}-05$	$2.29\text{E}+00$
400	4.8837	28934	$1.05\text{E}+20$	$4.47\text{E}-37$	$2.94\text{E}-05$	$2.47\text{E}+00$
600	4.6869	22026	$1.01\text{E}+20$	$3.70\text{E}-37$	$2.33\text{E}-05$	$2.50\text{E}+00$

12 % Mn-doped ZnO

A new target of 12 % doped ZnO was prepared by using the solid-state reaction method. Thin films from the target were grown using PLD system on sapphire (Al_2O_3) substrate at room temperature and at 600°C in an ambient 10 mTorr of oxygen. The X-ray diffraction on the films shows that films grown at room temperature (RT) are amorphous whereas the ones grown at 600°C have peaks corresponding to ZnO. In addition, these films also have impurity peaks of MnO_2 (Fig. 25).

Magnetization data are presented in Fig. 26. In comparison to 2% Mn-doped ZnO films, it is clear that the saturation magnetization of the 12% doped film is reduced by almost 50%. Precipitation of the antiferromagnetic MnO_2 impurity phases, as seen in the x-ray diffraction, is the primary reason for this reduction. Although the doping was at 12%, the electron dispersive x-ray spectroscopy (EDS) analysis showed that the Mn concentration in these films was around 6%. However, due to the impurity peaks in the x-ray diffraction spectrum, we could not apply the RKKY model.

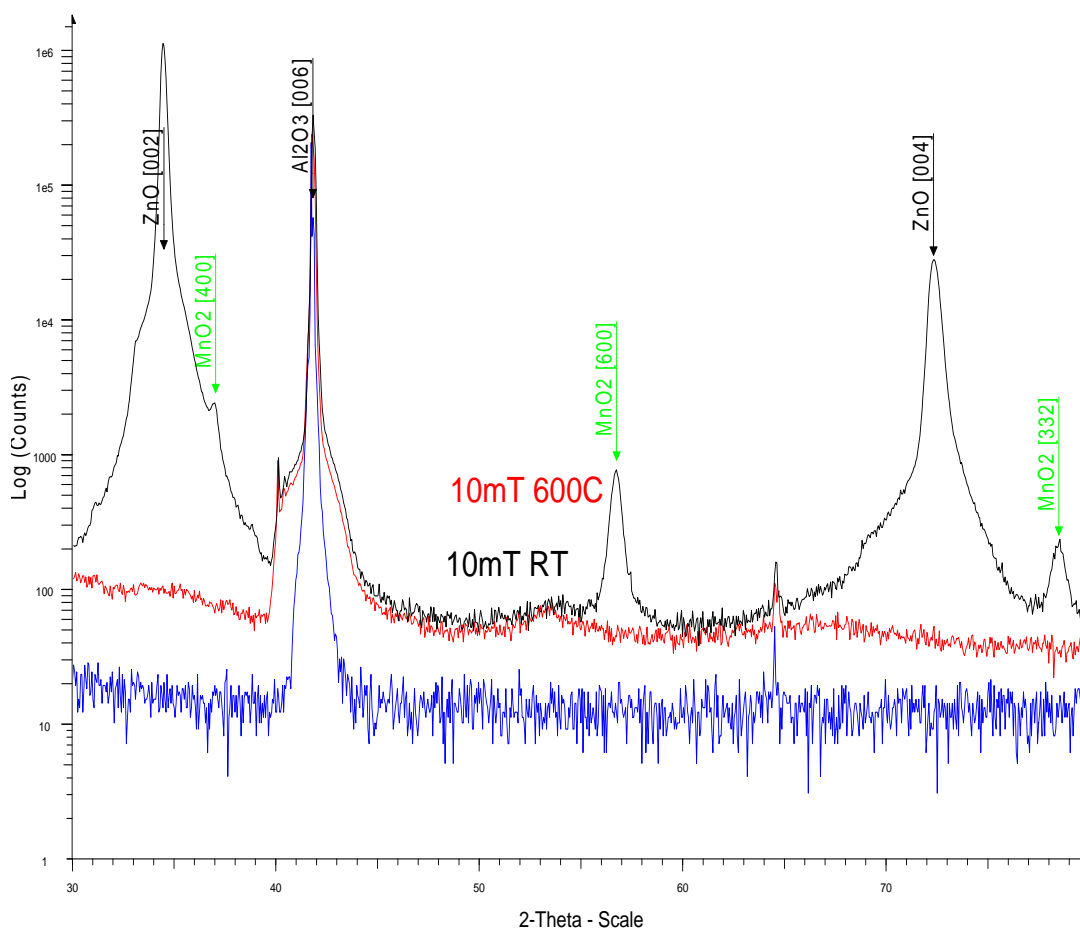


Figure 25: X-ray diffraction spectra of 12% Mn doped ZnO thin films grown at room temperature (black) and 600°C (red) with 10mTorr of oxygen pressure.

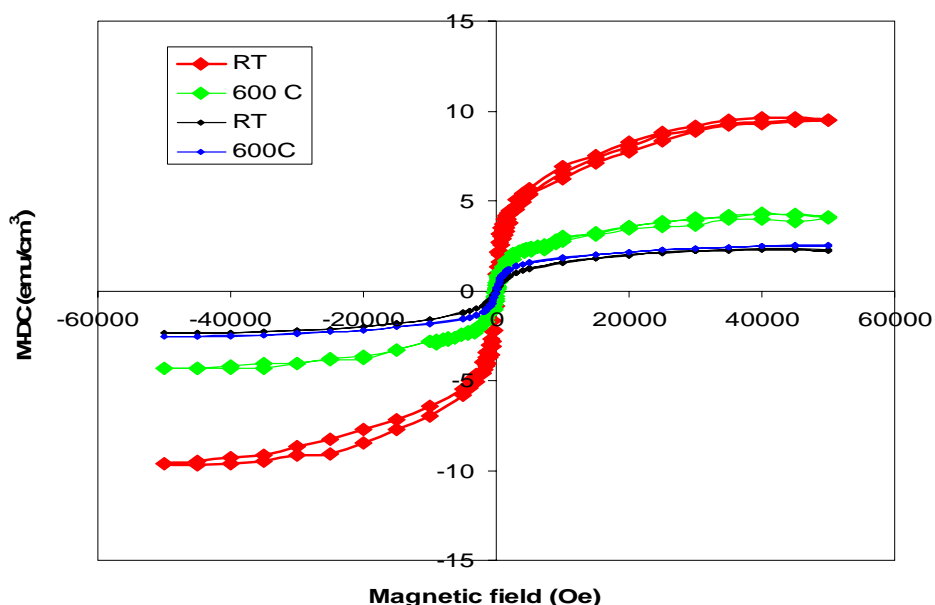


Figure 26: M-H loops at 10K of 2% Mn-doped (red and green) and 12% Mn-doped ZnO (blue and black) thin films grown on sapphire (Al_2O_3).

Ferroelectricity in epitaxial V-doped ZnO thin films deposited at high oxygen pressure

We observed the ferroelectricity in V doped ZnO films in the last report. Doping divalent Zn sites by pentavalent V ions creates a mixed valency as well as strain in the original ZnO hexagonal structure because of the reduced ionic size of vanadium. The mixed valency creates charge polarity between Zn-O and V-O bonds. This charge polarity and the rotation of the nonlinear V-O bonds w.r.t. Z-O bonds under electric field gives enhanced ferroelectricity [38, 39]. One of the factors that affects the polarizability of these films is the film conductivity. Presence of oxygen vacancies in ZnO gives rise to n-type conductivity and the resulting leakage currents reduce the polarization. We have grown epitaxial V-doped ZnO film under high oxygen pressure, from 100 mTorr to 500 mTorr, to increase the oxygen content of the films. The films with higher oxygen pressure are more insulating than the one grown with lower oxygen pressure. The saturation polarization is higher for the film grown at higher pressure as shown in Fig. 27 below. The saturation and remnant polarization are comparable to the values obtained previously [39]. Subsequently, bilayers of Mn-doped and V-doped ZnO have been grown to investigate the magneto-electric coupling between these ferromagnetic and ferroelectric layers.

ZnO:Mn/ZnO:V heterostructure

By using magnetic Mn-doped ZnO and ferroelectric vanadium (V) - doped ZnO, a bilayer Mn:ZnO/V:ZnO film was grown on a sapphire substrate. First, a 300 nm thick conducting undoped ZnO layer was epitaxially grown on sapphire substrate as the bottom electrode for poling. Successive Mn:ZnO and V:ZnO films with individual thicknesses of about 500 nm were grown. X-ray diffraction studies showed the heterostructure to be epitaxial with (0002) orientation where the FWHM of the (0002) peak was around 1° (Fig. 28).

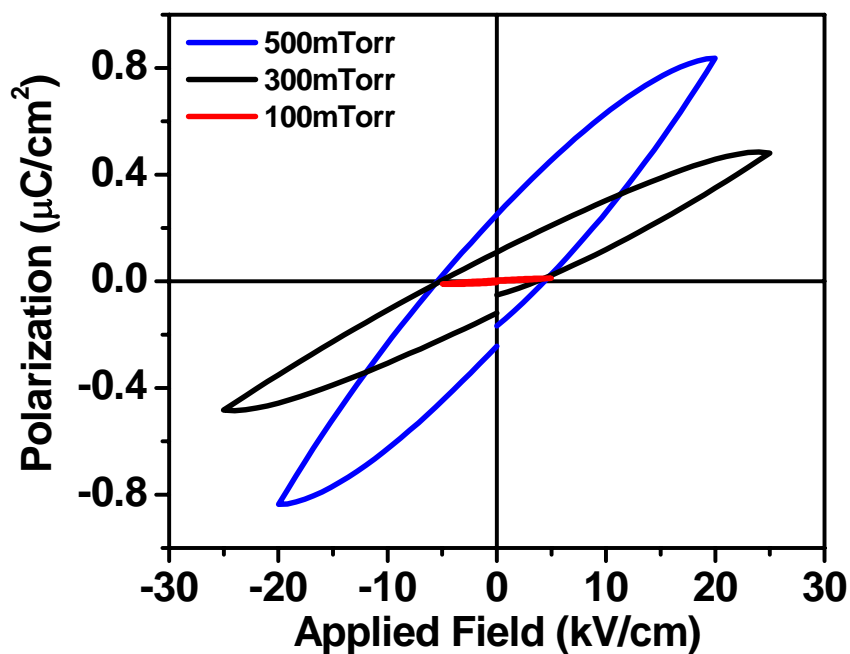


Figure 27: Polarization of three V doped ZnO films grown at different oxygen pressures.

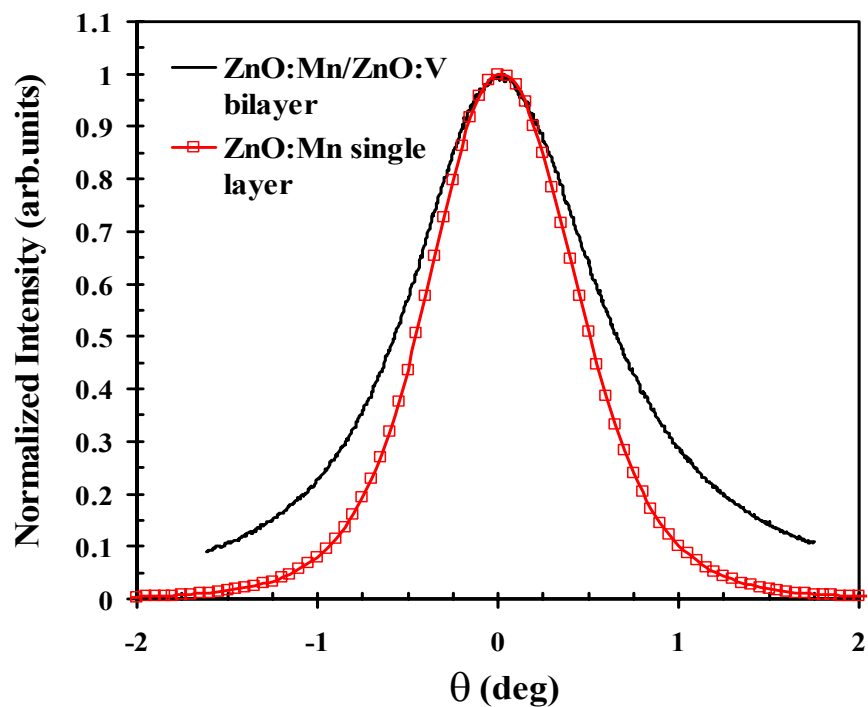


Figure 28: Rocking curves about the (0002) plane of ZnO. FWHM for ZnO:Mn single layer is 0.962° and for ZnO:Mn/ZnO:V bilayer is 1.158° .

Magnetization measurements on this bilayer film were done before and after poling. The poling was done at room temperature with amplitude of 5V. Since the magnetic measurements were done at 300K, poling was done at slightly higher temperature to avoid the loss of polarization due to thermal agitation. Fig. 29 shows M-H loops before and after poling. The decrease in the saturation magnetization is a clear evidence of the coupling between magnetic and ferroelectric layers.

In summary, a systematic study of the interfacial stress at the CFO and PZT film interfaces and the stress at the film-substrate interfaces has enabled us to understand the magnetic anisotropy that produces steps in the magnetization curves. This understanding is valuable as stress plays a major role in the manifestation of the multiferroic coupling between the ferromagnetic and the ferroelectric films. Investigation of Mn-doped ZnO films revealed that at low doping levels, such as 2%, Mn is substituted in place of Zn in the ZnO structure. The resulting magnetism can be explained via RKKY interaction between the conducting electrons and magnetic ions. However, for high doping percentages, such as 12%, precipitation of the antiferromagnetic phase MnO_2 decreased the overall magnetization of the films. We have also fabricated ZnO:Mn/ZnO:V heterostructures and demonstrated possible magnetoelectric coupling between the layers.

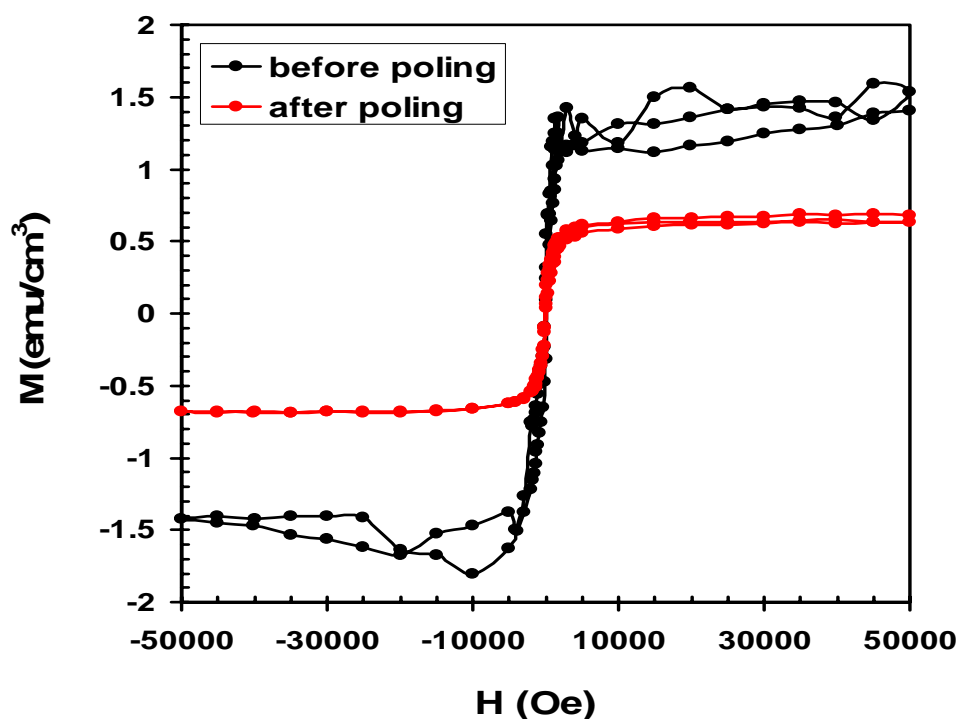


Figure 29: Magnetization loops at 300K before and after poling the ZnO:Mn/ZnO:V epitaxial heterostructure. M-H loops at 10K of 2% Mn doped (red and green) and 12% Mn doped ZnO (blue and black) thin films grown on sapphire (Al_2O_3).

Flexible photonic materials for solar-based energy sources

Quantum dots (QD) of PbSe and PbS have been shown to produce multiple excitons with the absorption of a single photon. Efficient dissociation of these excitons will produce a high density of charge carriers. A solar cell based on QDs has the potential to produce very large currents leading to conversion efficiencies well above the thermodynamic limit. In this project we are investigating the possibility of producing efficient solar devices that are flexible and cost-effective by combining QDs with semiconducting polymers.

Film morphology

In this study QDs of PbSe are grown by a solvothermal technique. Subsequently, the QDs are dispersed in heptanes and used as a precursor in the Laser-Assisted Spray (LAS) system to deposit surfactant-free PbSe QD films on substrates. The LAS process was described in last year's annual report.

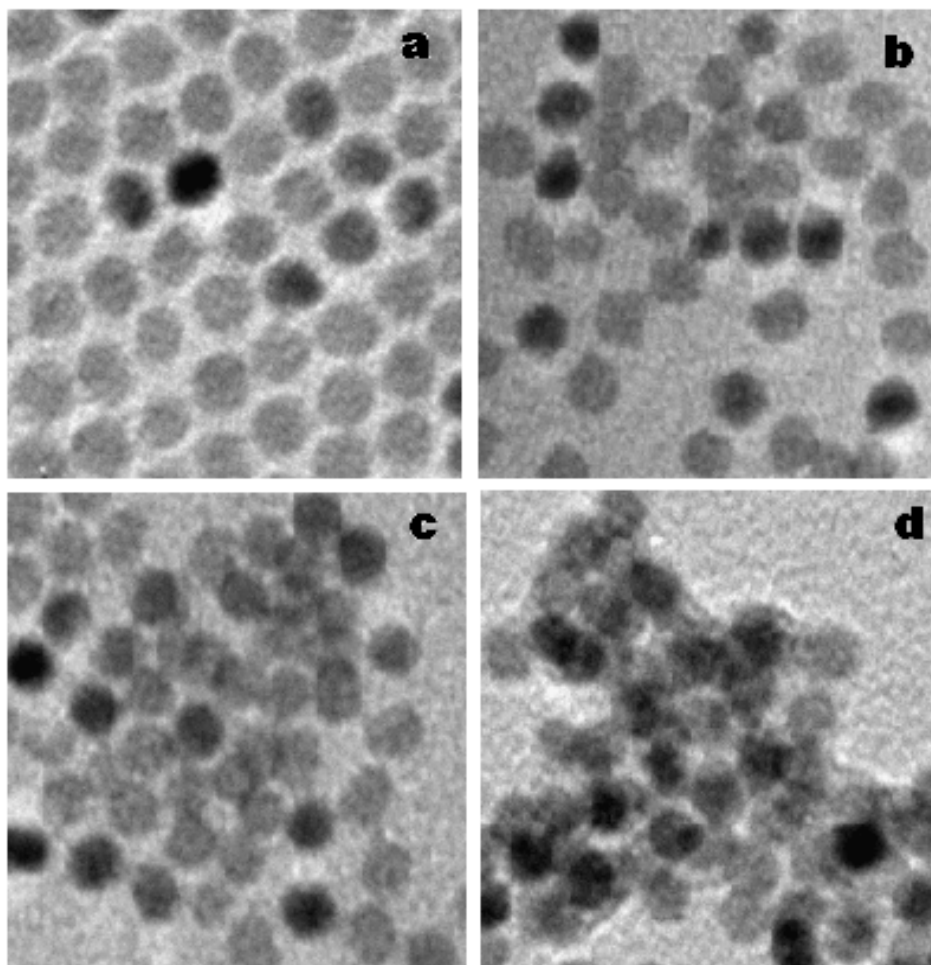


Figure 30: TEM images of PbSe QDs deposited on carbon coated TEM grid for 1min with different plume temperatures. (a) drop-casted (b) 80-100°C (c) 150-200°C (d) 200-230°C.

Fig. 30 shows TEM images of PbSe QDs deposited on carbon grids at different SF₆ flow rates. We have established a correlation between the flow rate and the temperature of the gas after laser heating. Since the amount of laser energy absorbed by the gas is related to the interaction time between the laser and the gas volume, high flow rates lead to lower temperatures. When the temperature of the plume was above 200°C, PbSe QDs tend to agglomerate while temperatures below 100°C do not seem to remove the surfactants completely. Optimum temperature where most of the QDs become connected without significant agglomeration was in the range of 150-200°C. The high-resolution TEM images (Fig. 31) clearly show intimate contact between QDs while drop-casted film shows 2nm gaps between them. QDs deposited by this method are distributed uniformly over a large area of the film. Distribution of QDs in a film is shown by the low-resolution TEM image in Fig. 32.

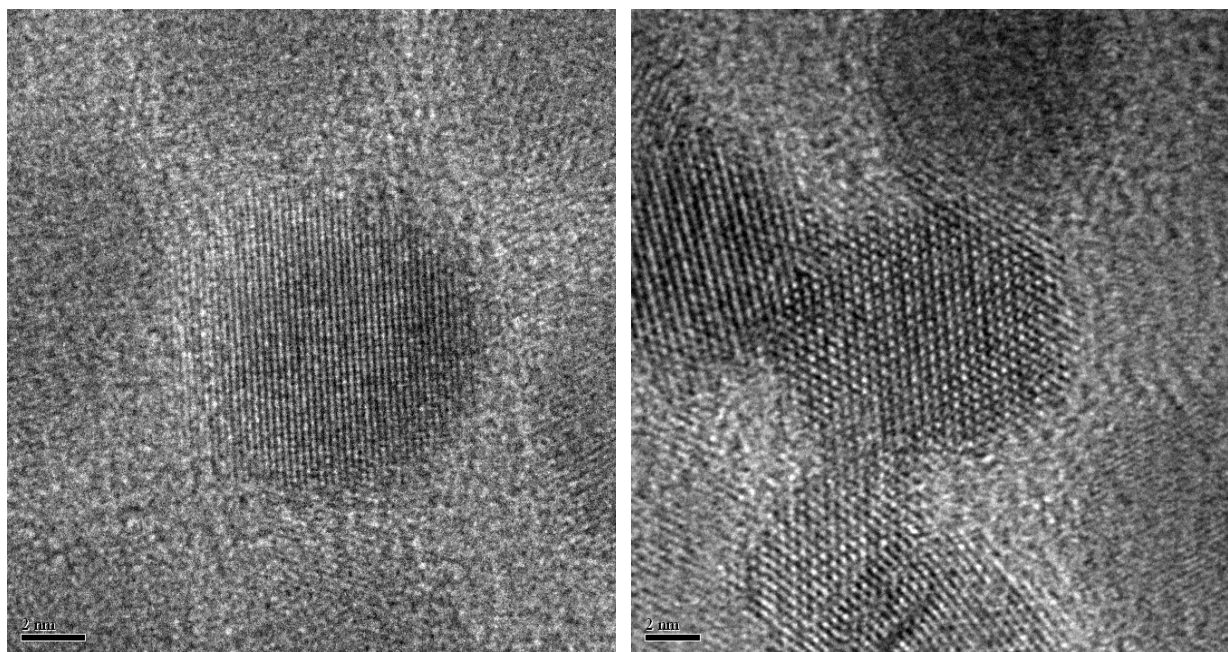


Figure 31: High resolution TEM images of (a) drop-casted and (b) LAS deposited PbSe NCs. LAS shows intimate contact between the NCs while the drop-casted film shows a 1-2nm surfactant coating between them.

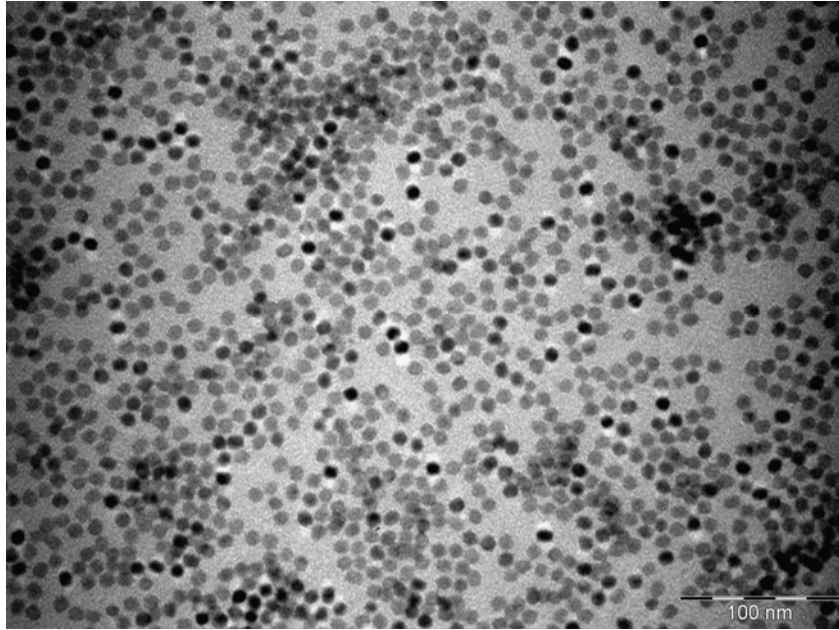


Figure 32: Low-resolution TEM image of PbSe QDs deposited on a TEM grid by the LAS process

Photocurrent Measurement

The DC photocurrent measurements of films were conducted by forming the structure shown in Fig. 33. Details of the structure formation were described in our previous report. Fig. 34 shows the current response of the surfactant-free PbSe QDs device under illumination by white light. The different shapes in positive and negative voltage sides were observed due to

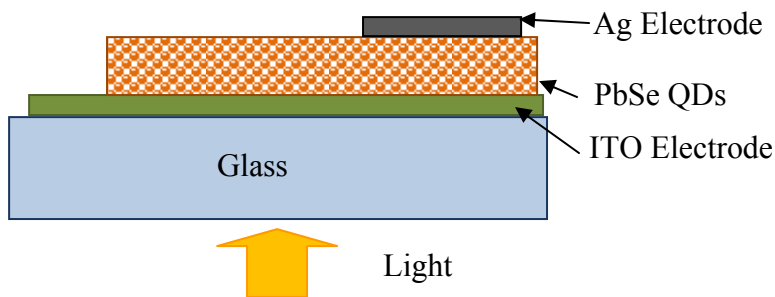


Figure 33: PbSe QD films structure deposited by Laser Assisted Spray (LAS) technique for photocurrent measurements.

different work functions of the electrodes. The positive side forms a Schottky barrier at Ag (4.74eV) and PbSe (4.2eV) junction while negative side forms a near ohmic contact at PbSe (4.82 eV) and ITO (4.6eV) junction. This Schottky barrier formation can be described by a simple diode equation:

$$I = I_s \left[\exp\left(\frac{qV}{nk_B T}\right) - 1 \right] \quad (8)$$

where I_s is the saturation current, q is the electronic charge, V is the potential drop across the junction, n is the ideality factor, k_B is a Boltzmann's constant, and T is the temperature.

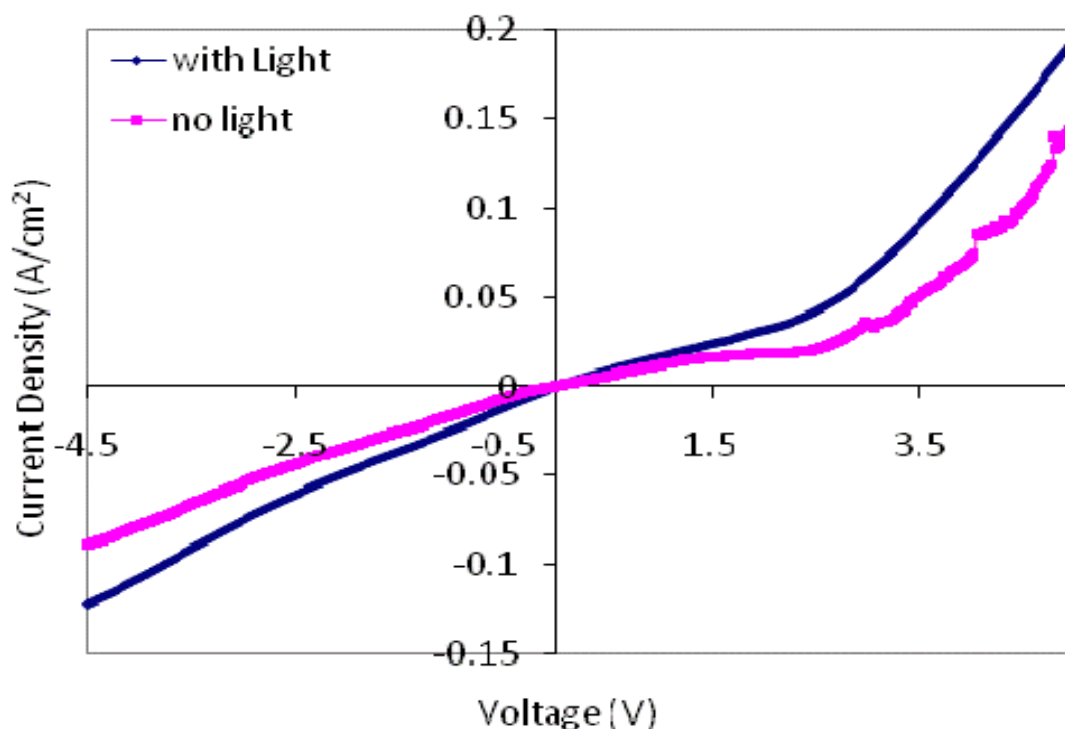


Figure 34: The graph of applied voltage vs. current density through surfactant free PbSe quantum dots film.

Photo-Generated Current by Laser Excitation

We have used a more sensitive technique to measure the photocurrent generated by the films by using diode laser excitation (wavelength of 670 nm). The photocurrent was measured

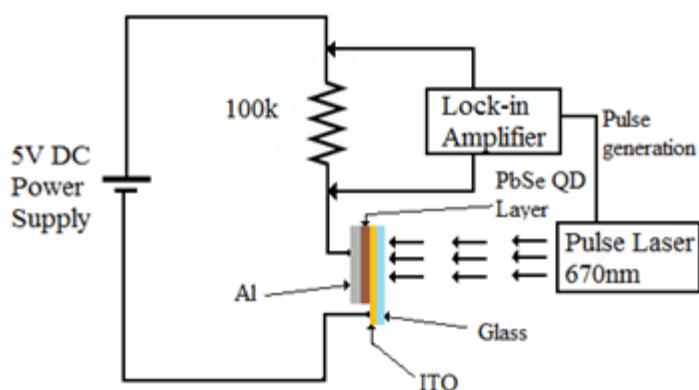


Figure 35: Circuit diagram for detecting photocurrent generated by the diode laser.

with various laser-pulse intensities under a constant bias voltage applied between the device electrodes. The circuitry used for these measurements is shown in Fig. 35. Generated electron and holes drift to opposite electrodes due to applied electric field across the device structure and flow out of the external circuit as a photocurrent. The generated photocurrent was measured with a lock-in amplifier synchronized with the pulse laser. The laser power was changed from 0

to 4.2mW by changing the input voltage to the device from 0 to 5V.

This circuit allows isolation of the current generated by the pulse laser. Since the lock-in amplifier can extract a signal with a known carrier wave frequency from a synchronized source, only the signal generated due to photo-generated carriers would be measured. The measured voltage across the series resistor is used to compute the generated current.

Characterization of P3HT polymer coatings

Crystallinity of the P3HT polymer was characterized by X-Ray Diffraction method. Since P3HT has very low-angle peaks, the scanning angles were set from 4° to 30° with 0.02 increments in 3sec/steps. Fig. 36 shows the XRD pattern of the P3HT polymer film that was deposited on a glass substrate by the LAS technique. XRD pattern clearly shows crystalline peaks corresponding to P3HT polymer. This is very similar to XRD patterns observed for

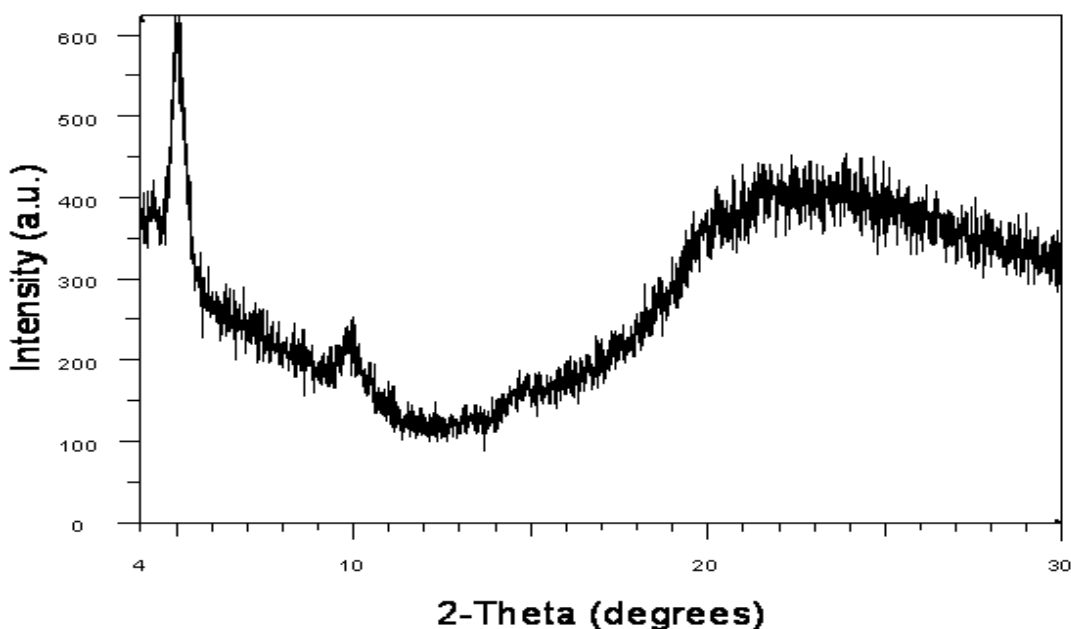


Figure 36: XRD pattern of P3HT polymer coating deposited by LAS technique on glass substrate heat up to 60°C .

coatings of this material fabricated by spin-coating technique [40,41]. Therefore it confirms that high-quality P3HT polymer can be deposited by LAS technique.

Photo-Generated Current in polymer films

The experimental set up (Fig. 33) described in an earlier section was used to determine the photo-generated current in the P3HT polymer layer that was sandwiched between ITO and Al electrodes. As described in the previous section the pulsed laser was used to excite electrons into the conduction band. The graph in Fig. 37 shows the photo-generated current recorded at various laser powers. The wavelength of the laser at 670 nm has photon energy of 1.85eV which is lower than the band gap of P3HT (1.97eV). Therefore, the measured current mainly corresponds to the carriers generated by exciton dissociation.

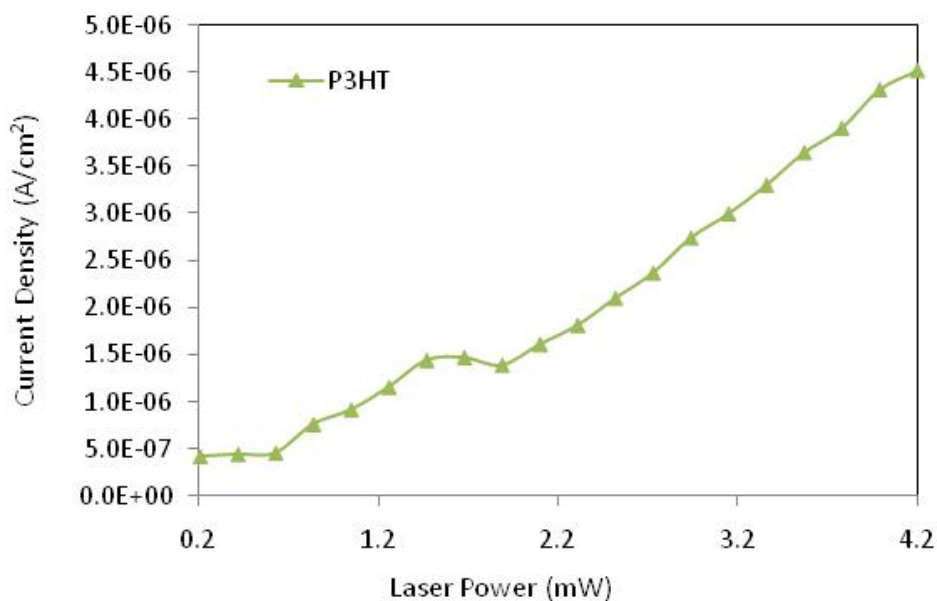


Figure 37: The graph of photo-generated current in the P3HT layer sandwich between ITO and Al electrodes at various laser power levels.

Characterization of PbSe QDs/P3HT Hybrid Composites

PbSe QDs/P3HT hybrid composite structures were fabricated by co-deposition of PbSe QDs

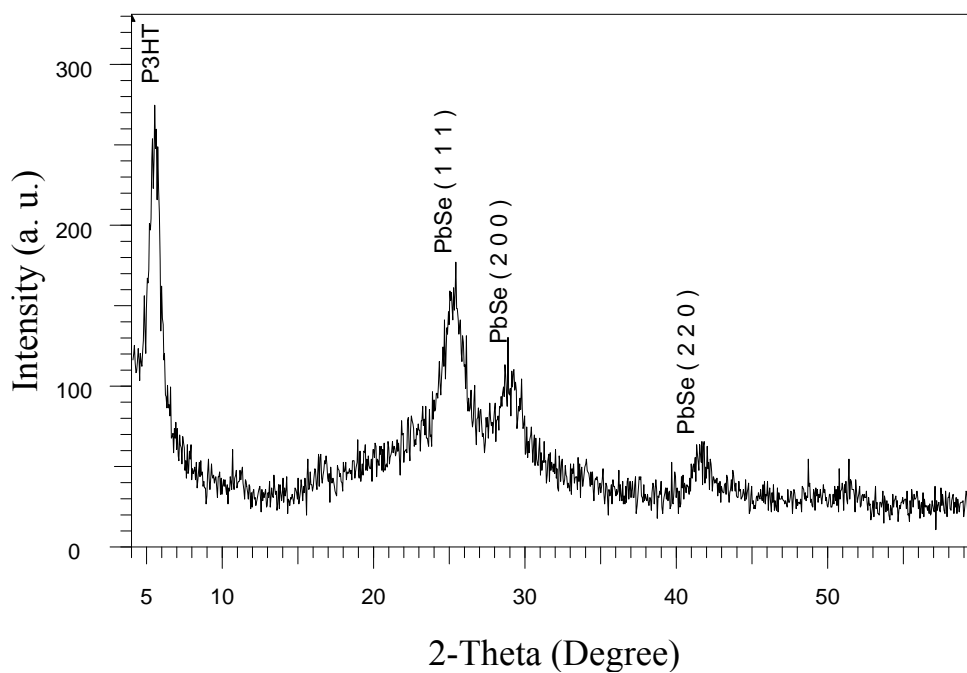


Figure 38: XRD pattern of PbSe QDs/P3HT hybrid composite deposited by laser assisted co-deposition.

and P3HT polymer films by the LAS process. Two independent nozzles were used to spray the precursor containing QDs and the precursor containing the polymer onto a substrate to form the hybrid coatings. The crystallinity and the microstructure were studied by XRD and TEM.

The XRD results in Fig. 38 show the PbSe and P3HT crystalline peaks in the deposited film. P3HT shows sharp crystalline peaks corresponding to bulk crystallinity in the material,

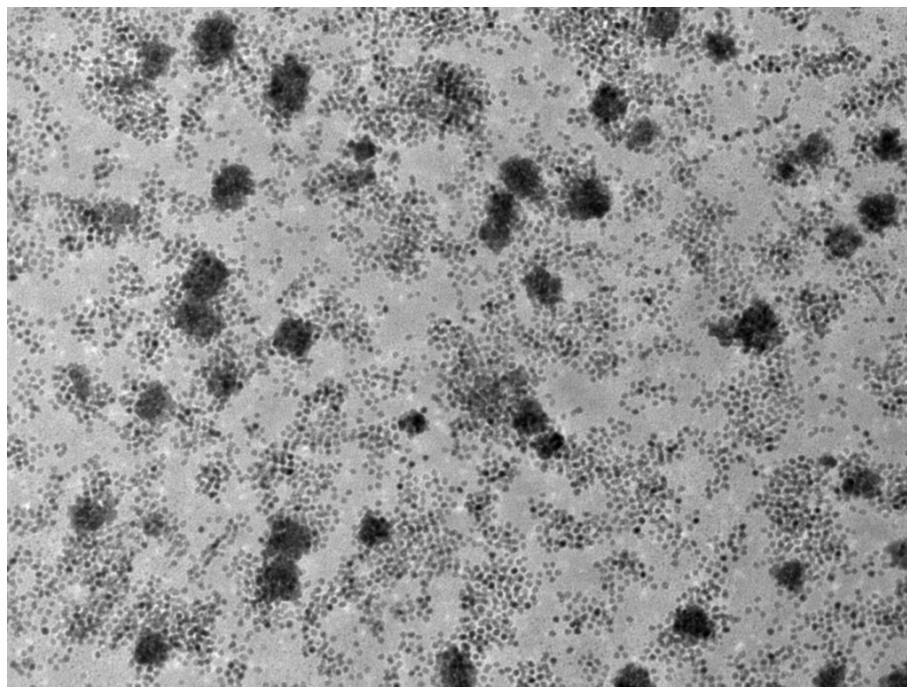


Figure 39: TEM image shows the initial formation of the composite P3HT polymer/ PbSe QD film in LAS co-deposition.

while PbSe shows broad peaks due to nanocrystallinity of the material. The TEM image obtained on carbon-coated grids shows the initial growth (Fig. 39). The dark areas represent QD/polymer mixtures. Only the very early part of the growth can be studied by this method as increasing thickness will not allow electron beam transmission.

Photo-Generated Current Measurements

The experimental set up shown in Fig. 33 was used to measure photo-generated current in the PbSe QDs/ P3HT polymer hybrid composite, which is sandwiched between ITO and Al electrodes. Fig 40 shows the change in photo-generated current in the PbSe QDs/ P3HT polymer composite with the laser power, and compares that with photocurrents generated in films of PbSe QDs and P3HT polymer. The enhancement in photocurrent in the composite structure results from the contributions of excitons generated in both QDs and the polymer.

Further investigation of the PbSe QDs/P3HT polymer composite was performed by using frequency-dependent photo-generated current measurements. The aim of this experiment was to study the internal capacitance of the composite layer that consists of the surfactant-free PbSe QDs and the P3HT polymer. Fig. 41 shows the frequency-dependent photo-generated current for a fixed average laser power. The photocurrent has also been calculated based on a model that follows the equivalent circuit that has been developed for the device.

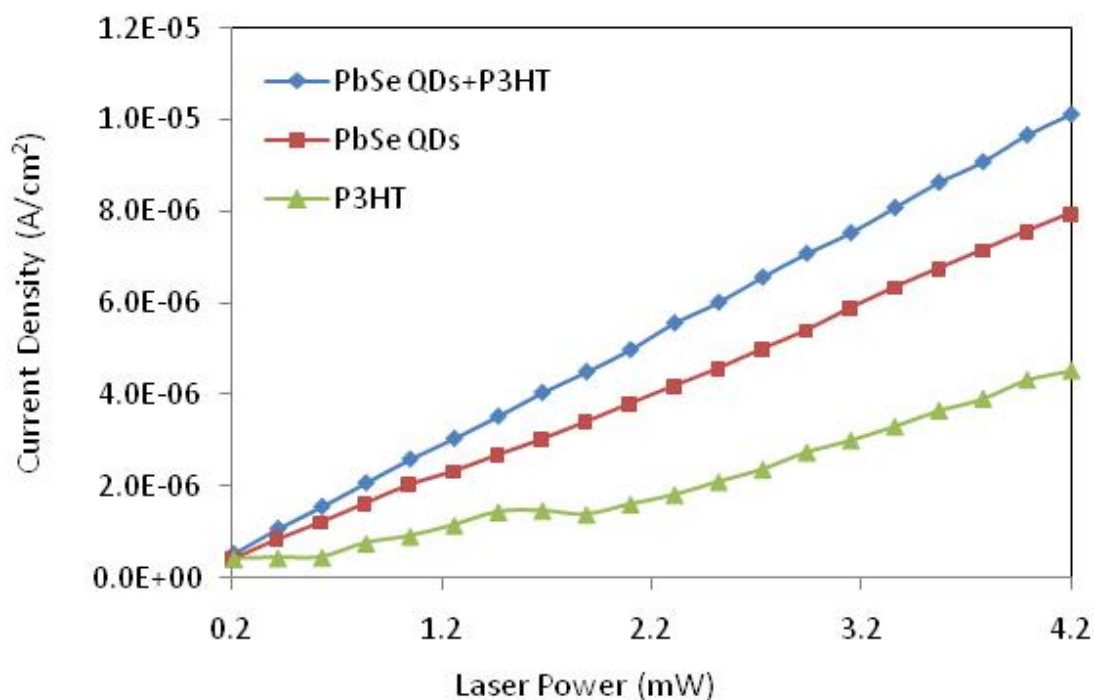


Figure 40: The graph of photo-generated current in the PbSe QDs/P3HT layer sandwich between ITO and Al electrodes at various laser power levels compared to PbSe QDs and P3HT polymer separately.

According to Fig.41 the photo-generated current across the device increases with increasing

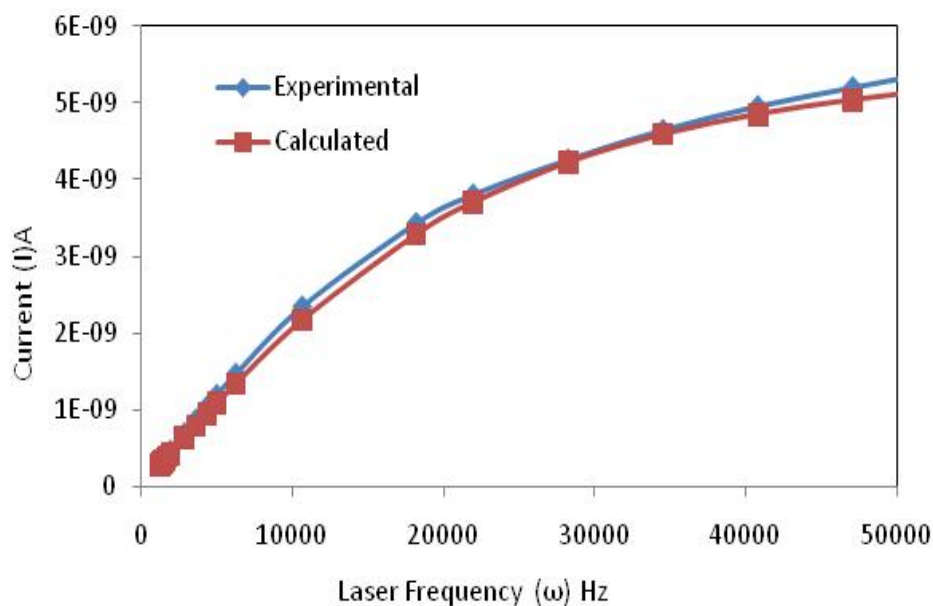


Figure 41: Calculated and experimental values of frequency dependent photo-generated current in PbSe QDs/P3HT polymer composite.

modulation frequency and approaches saturation. To account for the frequency dependence of the current the equivalent circuit of the device was taken as an RC circuit. The voltage and capacitor values for the equivalent RC circuit were obtained by using the experimental values.

The close agreement between the experimental results and the values computed based on the RC-circuit model (Fig. 42) allows us to derive the device built-in voltage and the capacitance. The values derived from a plot of $1/I^2$ vs. $1/\omega^2$ (Fig. 43) are $V_{RC}=5.773 \times 10^{-3}$ and $C=3.8 \times 10^{-10}$ F.

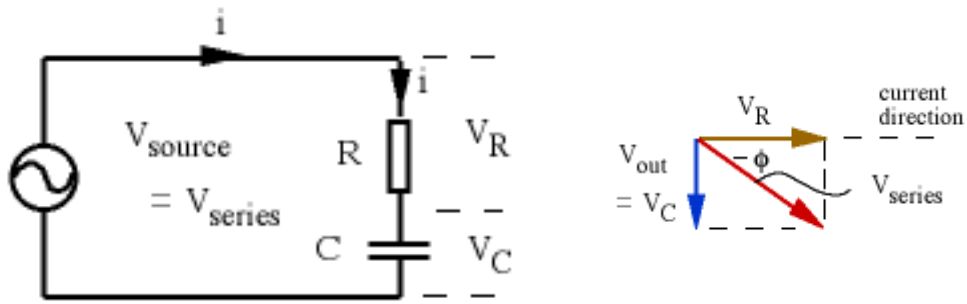


Figure 42: RC equivalent circuit of the photocell for analysis of the frequency dependence.

From Pythagoras' theorem:

$$V_{mRC}^2 = V_{mR}^2 + V_{mC}^2$$

$$V_{RC}^2 = V_R^2 + V_C^2$$

$$V_{RC}^2 = (IR)^2 + \left(\frac{I}{\omega C}\right)^2$$

$$V_{RC} = \sqrt{(IR)^2 + \left(\frac{I}{\omega C}\right)^2}$$

$$= I \sqrt{R^2 + \left(\frac{1}{\omega C}\right)^2}$$

$$\frac{1}{I^2} = \frac{1}{V_{RC}^2 \omega^2 C^2} + \frac{R^2}{V_{RC}^2} \quad (9)$$

So, using the resistance and the capacitive reactance $\frac{1}{\omega C}$

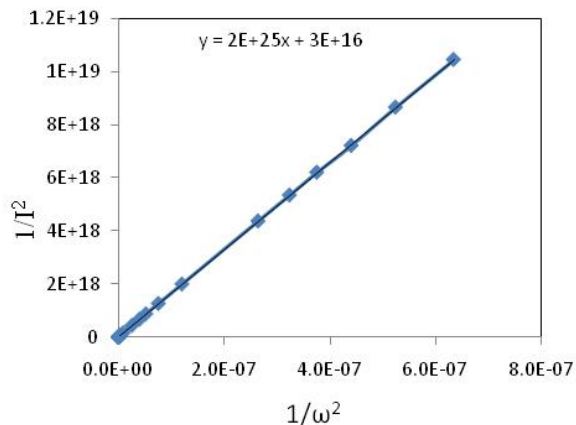
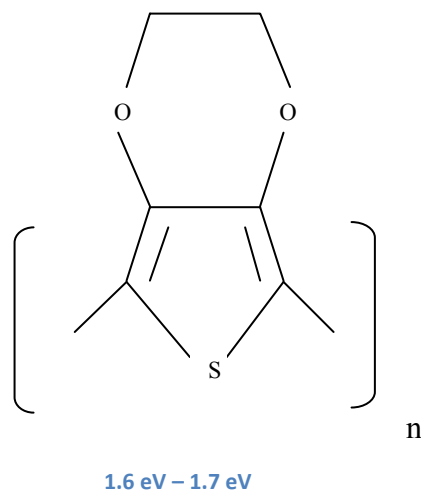


Figure 43: Graph of $1/I^2$ Vs $1/\omega^2$
From the $1/I^2$ Vs $1/\omega^2$ graph one can calculate source voltage (V_{RC}) and the capacitance (C). $V_{RC} = 5.773 \times 10^{-3}$ V and $C = 3.8 \times 10^{-10}$ F

In summary, PbSe QDs/P3HT hybrid composite structures were successfully fabricated by a co-deposition process. Investigation of PbSe QD/P3HT polymer composite structures with pulsed laser excitation showed frequency-dependent current generation. A simple RC circuit model enabled us to compute the built-in voltage and the capacitance of the device.

PbSe/TiO₂/PEDOT:PSS structure

In the fourth quarter of the second year, an alternative composite structure was sought that incorporated PbSe QDs in titanium dioxide (TiO₂) nanorods and polyethylenedioxythiophene (PEDOT). PbSe quantum dots (QDs) have been synthesized from a novel procedure with 2 nm average diameter. Smaller QD diameters are needed to tune the size of the PbSe QDs such that the band gap offset (0.35 eV) with the TiO₂ nanorods would preferentially inject electrons to allow ballistic transport to the fluorine-doped tin oxide (FTO) electrode. Several samples of TiO₂ nanorods of average length of 2 μ m and well-controlled density (for maximum PbSe monolayer distribution) have been prepared.



PEDOT sp^2 hybrid with double bonds which are shorter than single bonds (Pierelle's Instability).

Figure 44: Chemical structure of PEDOT:PSS, the polymer used to promote hole mobility in the solar devices.

Polystyrenesulfonate (PEDOT: PSS) has been chosen as the redox coupler in these structures (Fig. 44). PEDOT is sp^2 hybridized [42,43] and has a band gap of 1.6 -1.7 eV. Due to the Pierels instability the C – C bond length is greater than that of the C = C bond length, leaving

2 sub-bands, i.e. a completely filled valence (HOMO) and an empty conduction (LUMO) band separated by an energy gap. The primary transport mechanism in this polymer is known to be via hopping, with several orders of magnitude difference in the longitudinal and transverse directions.

The overall goal of this project is to fabricate an Al/PEDOT/PbSe/TiO₂/FTO hybrid

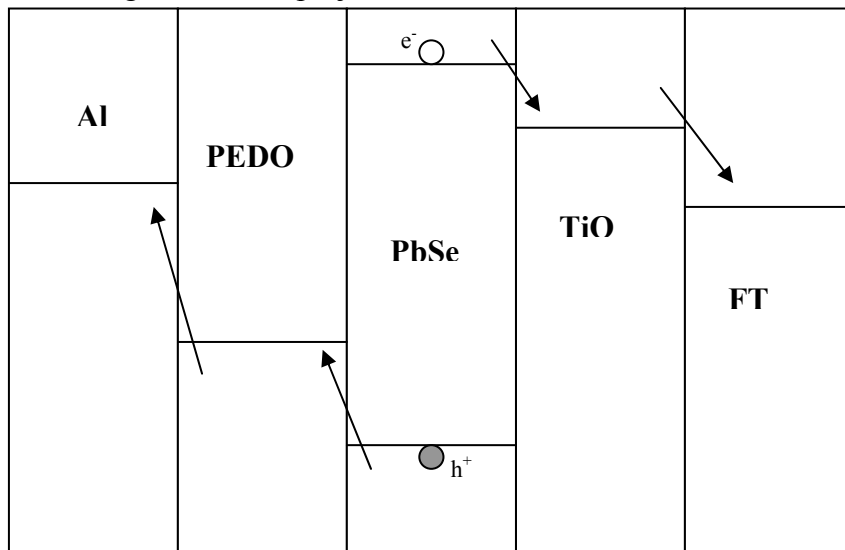


Figure 45: Expected band alignment in Al/PEDOT/PbSe/TiO₂/FTO structure that promotes efficient carrier transport across the device.

structure to effectively transport the photo-generated electrons and the holes. The band alignment of the cell components that enable charge transport within the structure is shown in Fig. 45. We have successfully fabricated TiO₂ nanorods on FTO-coated glass substrates by a solvothermal technique (Fig 46). The next step is to form the multilayer structure consisting of the 5 different components. A new Laser Assisted Spray deposition system with co-deposition capability has been constructed to fabricate all the subsequent layers of the hybrid structure (Fig. 47).

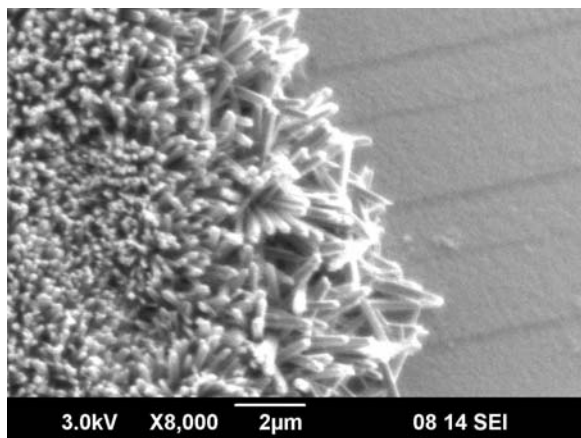


Figure 46: Titanium Dioxide nanorods (TiO₂) deposited on FTO-coated glass substrate



Figure 47: Laser-Assisted Spray deposition system for the fabrication of hybrid structures.

Task III: Solid-state materials for power conversion and refrigeration

High Performance nanofabricated thermoelectric materials for power generation

In our previous report, we demonstrated the successful synthesis of different nano-grain doped and undoped PbTe nanocrystals through various chemical processes. We densified the specimens by spark plasma sintering (SPS) [44,45]. We have since measured the low temperature transport properties of Bi-doped PbTe nanocomposites employing our custom-built transport measurement system. The results and discussion in the following sections are based on these studies.

Moreover, it is known that bismuth telluride alloys show the highest dimensionless figure of merit, ZT , in the room-temperature range, and are the materials most available in commercial thermoelectric cooling devices. Longstanding state-of-the-art $\text{Bi}_{2-x}\text{Sb}_x\text{Te}_3$ thermoelectric materials, at near room temperature operation, are $\text{Bi}_{0.5}\text{Sb}_{1.5}\text{Te}_3$ and $\text{Bi}_{0.5}\text{Sb}_{1.5}\text{Te}_{2.79}\text{Se}_{0.21}$ with high room temperature z value of $\sim 3.3 \times 10^{-3} \text{ K}^{-1}$ [46]. Recent research predicts that ZT can be improved by nanoscale effects [44,45,47]. Based on these predictions, we have synthesized undoped and different concentrations of Se-doped Bi_2Te_3 - Sb_2Te_3 based alloys by a chemical process. We have characterized these materials using X-ray diffraction (XRD), Scanning Electron Microscopy (SEM) and Energy Dispersive X-ray analysis (EDS). Preliminary results show phase purity of the specimens with small crystallite sizes.

Nanocrystal Synthesis

Doped PbTe nanocrystals of different sizes have been synthesized by low temperature reverse microemulsion and direct precipitation methods. Na-AOT, water and n-hexane, each of high purity grades have been used as the surfactant, water phase, and oil phase, respectively, for the microemulsion process. Pb-acetate, Na-tellurite and Bi-nitrate were used as the Pb, Te and Bi sources, respectively. A tellurium alkaline aqueous solution and lead acetate trihydrate were used for the direct precipitation process. The dark black precipitate in each case was filtered out by centrifugation repeatedly with water and ethanol. To dope the nanocrystals with different percentages of Bi ions, Bi-nitrate was added to the solution with Pb-source in calculated amounts (1-15% substitution for Pb) during the reaction. These reactions yielded products of > 2 gms per batch. The powders were first washed and then dried in a vacuum oven for 12 hrs, before XRD analysis. For transport property measurements, the specimens were densified via SPS, then cut into $2 \times 2 \times 5 \text{ mm}^3$ parallelepipeds. In the figures below, the specimens prepared by direct precipitation are referred to as DP and the specimens prepared by microemulsion are referred to as ME.

$\text{Bi}_{0.5}\text{Sb}_{1.5}\text{Te}_3$ and $\text{Bi}_{0.5}\text{Sb}_{1.5}\text{Te}_{2.79}\text{Se}_{0.21}$ nanocrystals were prepared by an ethylene-glycol (EG) mediated solvothermal route. Bi-nitrate, Sb-chloride, Na-tellurite and Se-dioxide were chosen as the Bi, Sb, Te and Se precursors, respectively. The reactions were carried out at 230°C for 12 hrs in custom built Teflon lined steel chambers. After the desired time, the reaction was terminated and the product was obtained by repeated centrifugation with water and ethanol.

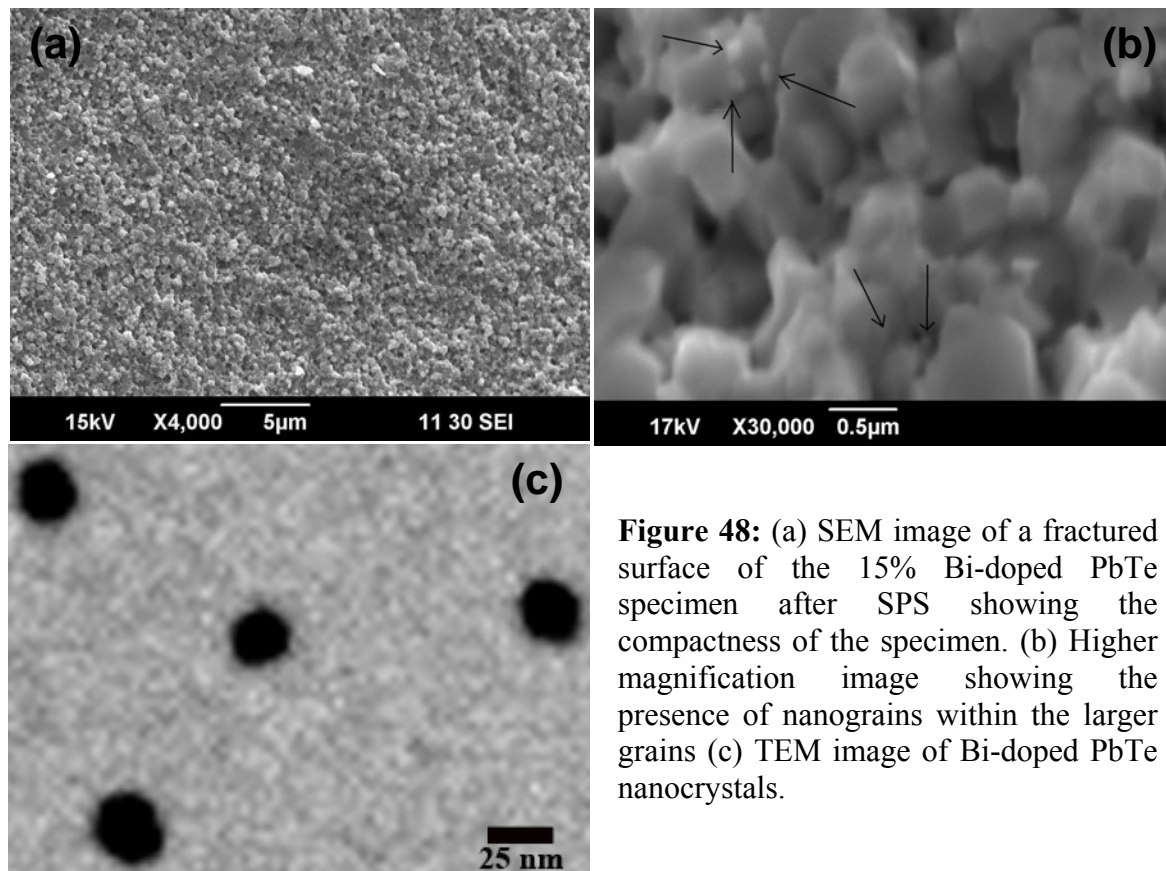


Figure 48: (a) SEM image of a fractured surface of the 15% Bi-doped PbTe specimen after SPS showing the compactness of the specimen. (b) Higher magnification image showing the presence of nanograins within the larger grains (c) TEM image of Bi-doped PbTe nanocrystals.

PbTe nanocomposites

XRD indicated the PbTe phase only, even for heavily doped PbTe nanoparticles. Impurities did not appear even after SPS. EDS performed on the densified pellets showed the presence of Bi in PbTe. Particle sizes calculated from the XRD spectra by the Debye-scherrer formula were $\sim 30\text{-}50\text{ nm}$ for nanoparticles synthesized in the microemulsion technique and $\sim 50\text{-}100\text{ nm}$ for nanoparticles synthesized by the direct precipitation technique.

Morphological features of the specimens were studied by SEM and transmission electron microscopy (TEM) and indicated the relative uniformity in the grain size distribution. These analyses indicated nanostructuring after densification. Fig. 48 (a) and (b) show the SEM images of the 15% Bi doped PbTe specimens after SPS. The high resolution SEM images indicate the presence of nanograins ($\sim 30\text{-}50\text{ nm}$) within larger grains. The average grain size of the specimens was estimated to be approximately 500 nm after SPS. The grain size of the synthesized specimens calculated from the low resolution TEM was $\sim 25\text{-}30\text{ nm}$ before SPS.

Temperature dependent four probe resistivity (ρ), steady-state Seebeck (S) and thermal conductivity (κ) were measured from 300 K to 12 K in a radiation-shielded vacuum probe. The undoped PbTe nanocomposite specimen was found to have positive S values for the entire temperature range investigated. Bi-doped specimens showed an increasing electrical conductivity with doping. Temperature dependent ρ , S and κ data for several specimens are shown in Fig. 49. From Fig. 49(a), $\Delta\rho/\Delta T > 0$ above 150 K , indicating metallic conduction above $\sim 150\text{ K}$, while $\Delta\rho/\Delta T < 0$ below 150 K . With increasing Bi concentration from $1\text{ mol}\%$ to $15\text{ mol}\%$, a systematic decrease in room temperature resistivity values were observed, presumably indicating higher electron concentrations with Bi doping. Fig. 49(b) shows S as a function of

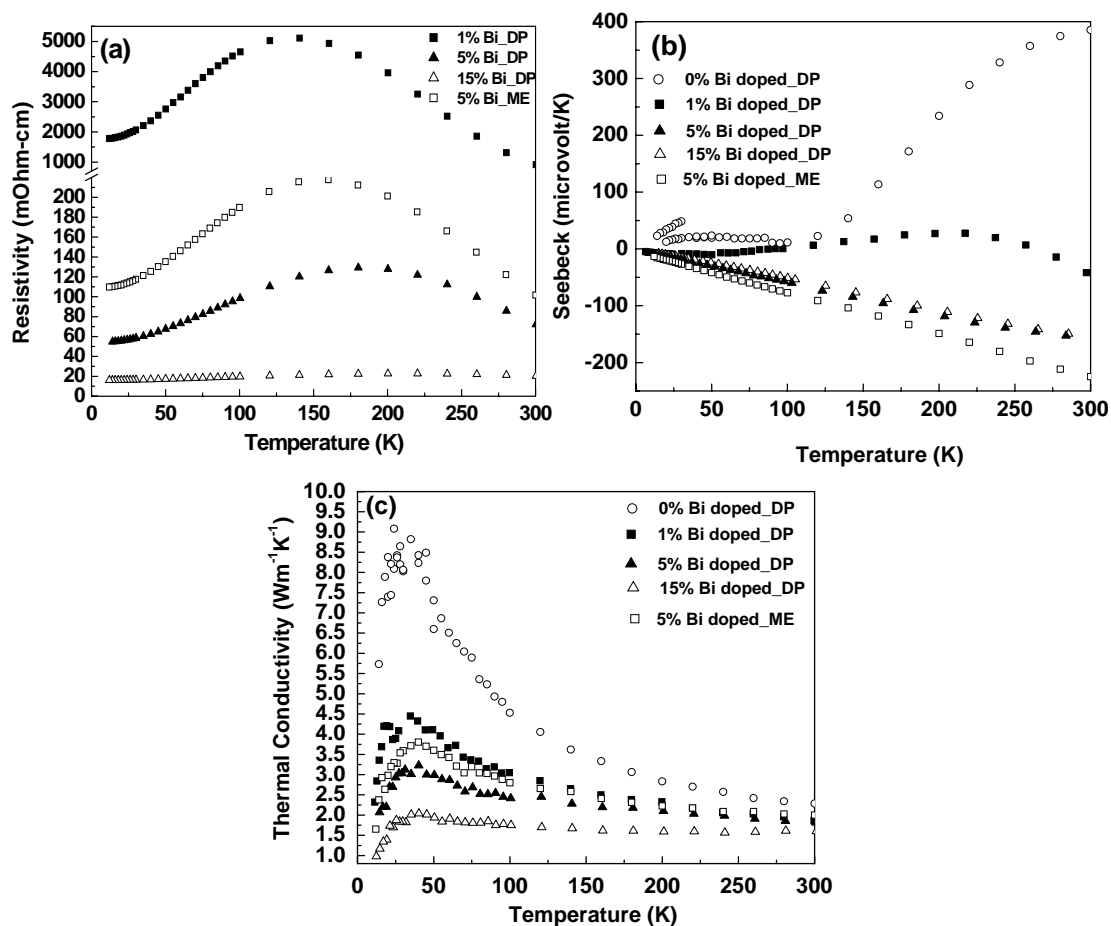


Figure 49: Temperature dependent (a) ρ , (b) S and κ data for representative undoped and Bi doped PbTe nanocomposites.

temperature for the Bi-doped PbTe specimens. The undoped PbTe nanocomposite shows positive S values, whereas the Bi-doped specimens show $S < 0$ suggesting an excess of electron carriers in the doped nanocomposites. For the 1% Bi-doped PbTe nanocomposite, conduction from contributions from holes and electrons may be present as can be assumed from the change in sign and slope ($\Delta S/\Delta T$) of S , in addition to the high ρ values. However, for higher concentrations of Bi, the PbTe nanocomposites show larger absolute S values and lower ρ , indicating an increased electron concentration. Hall measurements currently underway will reveal the doping in these specimens.

All the specimens show relatively low thermal conductivity values as shown in Fig. 49(c). The temperature dependence of κ for all specimens is similar to that of bulk polycrystalline PbTe with a maximum occurring between 20 K and 30 K. These features are indicative of a crystalline temperature dependence for the nanocomposites.

To further modify the electrical properties, we have prepared nanocomposites with higher concentrations (20 mol% and 25 mol%) of Bi. With these specimens, as well as Hall data, we expect to gain new insight into the doping of these nanocomposites as well as a complete evaluation of their thermoelectric properties.

Theoretical study of CoSb₃

In our previous report we have also carried out a theoretical study of the *p*-type PbTe nanocomposite materials and have predicted the conduction mechanisms and anomalies involved in the system. The theoretical model we have developed and applied to PbTe nanocomposites can be used to understand the transport properties in nanocomposites of different chemical composition providing the assumptions made initially are valid. The applicability of this phenomenological model is limited by diffusive carrier transport, relaxation time approximation, same electronic structure for the grains as bulk, and two-band Kane model for the bandstructure.

We suggest that carrier conductivity, σ , and S of granular composites made of skutterudite CoSb₃ can also be described by our theoretical model. For granular regions larger than the carrier mean free path, the electronic structure is similar to the electronic structure of bulk CoSb₃. Also, the bandstructure can be approximated by the two-band Kane model [48]. Using Eqs. [44,45] from Ref. [49], we can calculate the dependence of S and σ on the carrier concentration and various characteristics of the grains using the physical parameters for CoSb₃.

For CoSb₃ we find similar dependences as for the case of PbTe nanocomposites. For example, for longer grains, shorter barrier heights, and thinner barriers, σ is larger, but the S is smaller. For thermoelectric applications, however, we are interested in a large power factor, $PF = S^2\sigma$. Thus one must choose an optimal set of granular characteristics to achieve the highest PF . In Fig. 50, we show the power factor at different temperatures as a function of E_b , w , and L for the skutterudites. All scattering mechanisms are included and the concentration is $N_i=15\%$.

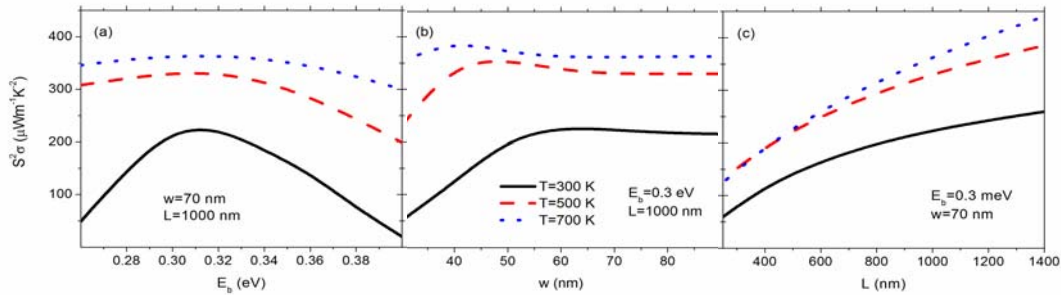


Figure 50: Power factor for CoSb₃ as a function of (a) barrier height E_b ; (b) barrier width w ; and (c) distance between the barriers L for different temperatures and $p=6.2 \times 10^{18}\text{ cm}^{-3}$.

Figure 50 shows that PF has similar behavior as that for PbTe. In particular, PF exhibits maxima for certain E_b and w . The maxima for PF vs. E_b is more pronounced for lower temperatures, while the maxima for PF vs. w is more pronounced at higher temperature. When L is changed, however, PF increases towards that for the bulk. Thus our model shows that for CoSb₃ it is possible to obtain an optimum set of parameters for improved thermoelectric performance due to the interplay between the grain interface scattering mechanism and the other scattering mechanisms, such as carrier-phonon and carrier-ionized impurity scattering mechanisms.

Currently, we are exploring different venues to further our understanding of the transport properties of granular nanocomposites. So far our focus was to model the carrier transport properties, such as σ and S . κ , however, is also of interest since it is explicitly found in ZT . κ has an electronic and lattice component, $\kappa = \kappa_e + \kappa_l$, respectively. κ_e will be calculated using similar expressions as that used for σ and S [50], while κ_l will be calculated using the Callaway model derived from the phonon Boltzmann equation of motion within the relaxation time

approximation for various phonon scattering mechanisms [51]. The emphasis will be on including the phonon scattering due to the grain boundaries explicitly.

Our goal will be to present comprehensive modeling of all transport parameters entering the ZT . Thus our study will answer questions directly related to the possibility of using nanocomposite materials with granular formations for higher ZT applications.

Nanocrystals of Bi-Sb-Te and Bi-Sb-Te-Se alloys

Solid solutions of Bi_2Te_3 and Sb_2Te_3 , $(\text{Bi}_x\text{Sb}_{1-x})_2\text{Te}_3$, increase the ZT value, as compared to the binary compounds, by reducing κ due to alloying [46]. Furthermore, σ can be increased by substituting Te with Se. Currently, bulk and nano-grain $\text{Bi}_2\text{Te}_3/\text{Se-Sb}_2\text{Te}_3/\text{Se}$ alloys are typically prepared by zone melting, Bridgman technology and ball milling processes [47,52,53]. However, powders prepared by a solution chemistry route are desirable due to the ease of processing. In addition, nanoscale inclusions are expected to result in improved thermoelectric properties over that of the bulk [47]. We have successfully synthesized $\text{Bi}_{0.5}\text{Sb}_{1.5}\text{Te}_3$ and $\text{Bi}_{0.5}\text{Sb}_{1.5}\text{Te}_{2.79}\text{Se}_{0.21}$ nanoparticles with a crystallite size of 18 ± 5 nm. The crystal structure and morphology of the nanocrystals were studied by XRD and SEM. Figure 51 shows the XRD pattern of the $\text{Bi}_{0.5}\text{Sb}_{1.5}\text{Te}_3$ nanocrystals indicating the phase purity with all the peaks matching the hexagonal

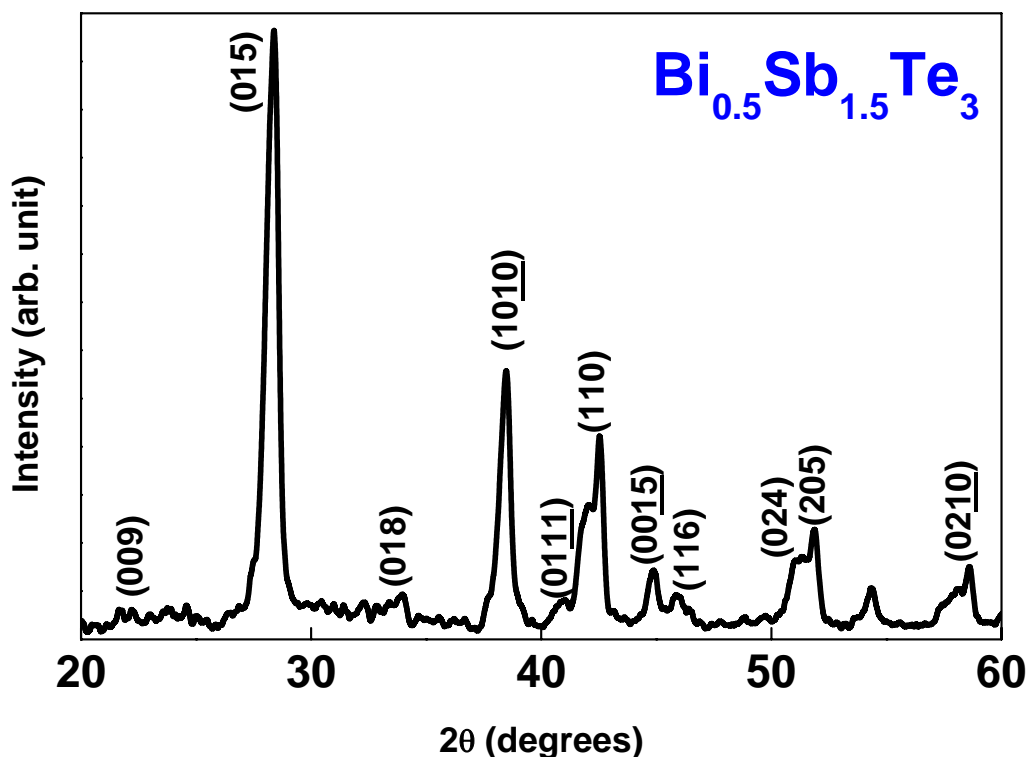


Figure 51: XRD pattern of the $\text{Bi}_{0.5}\text{Sb}_{1.5}\text{Te}_3$ nanocrystals prepared by ethylene-glycol mediated solvothermal process.

Bi_2Te_3 structure. $\text{Bi}_{0.5}\text{Sb}_{1.5}\text{Te}_{2.79}\text{Se}_{0.21}$ showed similar XRD spectra with no detectable secondary phases. This suggests that Se may have been introduced in the structure as a dopant. The

broadened diffraction peaks indicate that the particle size is small. This is corroborated by SEM analysis. The composition of the nanoparticle clusters has been analyzed by EDS indicating nearly stoichiometric compositions of $\text{Bi}_{0.5}\text{Sb}_{1.5}\text{Te}_3$ and $\text{Bi}_{0.5}\text{Sb}_{1.5}\text{Te}_{2.79}\text{Se}_{0.21}$. Figure 52 shows the EDS spectrum of $\text{Bi}_{0.5}\text{Sb}_{1.5}\text{Te}_{2.79}\text{Se}_{0.21}$ nanoparticles. Room temperature S measurements are positive for both specimens. To the best of our knowledge, this work is the first demonstration of $\text{Bi}_{0.5}\text{Sb}_{1.5}\text{Te}_3$ and $\text{Bi}_{0.5}\text{Sb}_{1.5}\text{Te}_{2.79}\text{Se}_{0.21}$ synthesized by this method.

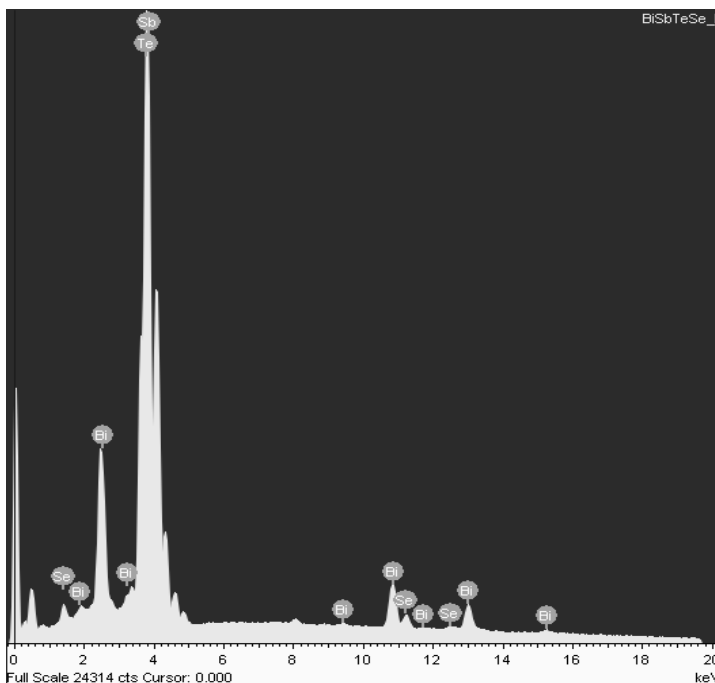


Figure 52: A typical EDAX spectrum of the prepared $\text{Bi}_{0.5}\text{Sb}_{1.5}\text{Te}_{2.79}\text{Se}_{0.21}$ nanocrystals revealing near stoichiometric Bi, Sb, Te and Se (0.45:1.5:2.8:0.19) ratio.

The research is going according to the scheduled tasks. In continuation of our work we plan to measure the low temperature transport properties of the Bi-doped PbTe and Bi_2Te_3 alloy nanocomposites outlined before. A systematic investigation of the morphology and thermoelectric properties at elevated temperatures as well as core-shell morphologies are also planned. Theoretical investigations in corroboration with, as well as guiding of, the experimental work will continue.

III. Reportable Outcomes

Publications and presentations based on support through grant USAMRMC W81XWH-07-1-0708 (*CIFM-supported researchers are shown in bold with PIs underlined*):

Journal Publications (Published/Submitted):

1. “Carbon Nanostraws: Nanotubes filled with superparamagnetic particles” **S. Pal**, S. Chandra, M. H. Phan, **P. Mukherjee** and **H. Srikanth**, Nanotechnology (in press, 2009)
2. “Critical length and giant magnetoimpedance in Co-Fe-Ni-Si-B amorphous ribbons” **A. Chaturvedi**, A. –T. Le, M. –H. Phan and **H. Srikanth**, Journal of Applied Physics (under review 2009)
3. “Chemical synthesis and magnetic properties of cubic CoO nanocrystals and 3D nanostructures” –V. Alexandrakis, G. Basina, D. Niarchos, G. Hadjipanayis, **S. Pal**, **H. Srikanth**, I. Panagiotopoulos, V. Tzitzios, Crystal Growth and Design (in press, 2009)
4. “Magnetism and magnetocaloric effect in gadolinium-iron garnet nanostructures” –M. H. Phan, **M. B. Morales**, C. N. Chinnasamy, V. G. Harris and **H. Srikanth**, Journal of Physics D: Applied Physics 42, 115007 (2009)
5. “Preparation of nearly monodisperse nickel nanoparticles by a facile solution based methodology and their ordered assemblies” –D. Sidhaye, T. Bala, S. Srinath, **H. Srikanth**, P. Poddar, M. Sastry and B. L. V. Prasad, Journal of Physical Chemistry 9, 113 (2009)
6. “Synthesis and magnetic properties of gold-coated iron oxide nanoparticles” **S. Pal**, **M. B. Morales**, **P. Mukherjee**, **H. Srikanth**, Journal of Applied Physics 105, 07B504 (2009)
7. “Particle blocking and carrier fluid freezing effects on magnetic properties of Fe₃O₄-based ferrofluids” –**M. B. Morales**, M. H. Phan, **S. Pal**, N. A. Frey and **H. Srikanth**, Journal of Applied Physics 105, 07B511 (2009)
8. “Inter-particle interactions in coupled Au-Fe₃O₄ nanoparticles” - N. A. Frey, M. H. Phan, **H. Srikanth**, S. Srinath, C. Wang, S. Sun, Journal of Applied Physics 105, 07B502 (2009)
9. “Long range ferromagnetism and giant magneto-caloric effect in type VIII Eu₈Ga₁₆Ge₃₀ clathrates” –M. H. Phan, G. T. Woods, **A. Chaturvedi**, **G. S. Nolas**, **H. Srikanth**, Applied Physics Letters 93, 252505 (2008)
10. “Static and dynamic magnetic properties of Co nanoparticles” –S. Srinath, P. Poddar, D. S. Sidhaye, B. L. V. Prasad, J. Gass and **H. Srikanth**, Journal of Nanoscience and Nanotechnology 8, 4086 (2008)
11. “Interface interaction between thin films of transition metal compounds and silicon substrates across the native SiO₂ layer”, **S. Witanachchi**, H. Weerasingha, H. Abou Mourad, and **P. Mukherjee**, Physica B (in press, 2009).
12. “Enhanced charge-transport in surfactant-free PbSe quantum dot films grown by a laser-assisted spray process”, **G. Dedigamuwa**, X. Jiang, J. Zhang, **P. Mukherjee**, and **S. Witanachchi**, Appl. Phys. Lett. 95, 122107 (2009).
13. “Intrinsic magnetic phases in cobalt ferrite thin films grown on silicon substrate by pulsed laser ablation”, **T. Dhakal**, **D. Mukherjee**, **P. Mukherjee**, **H. Srikanth**, and **S.**

- Witanachchi**, Journal of Appl. Phys. (Submitted in Jun. 2009).
14. "Growth of epitaxial ZnO:Mn/ZnO:V heterostructures and ferroelectric-ferromagnetic characterization", **D. Mukherjee**, **T. Dhakal**, **R. Hyde**, **P. Mukherjee**, **H. Srikanth**, and **S. Witanachchi**, Proceedings of the Materials Research Society Meeting, April 2009.
 15. "A model of transport properties of Thermoelectric nanocomposite materials", A. Popescu, **L.M. Woods**, **J. Martin**, and **G.S. Nolas**, Physical Review B 79, 205302 (2009).
 16. "Enhanced Seebeck coefficient through energy barrier scattering in PbTe nanocomposites", **J. Martin**, L. Wang, L. Chen, and **G.S. Nolas**, Physical Review B 79, 115311 (2009).
 17. "Synthesis and thermoelectric properties of lead chalcogenide nanocomposites", **J. Martin**, S. Stefanoski, L. Wang, L. Chen and **G.S. Nolas**, Mat. Res. Soc. Symp. Proc. 1044, 13 (2008).
 18. "PbTe nanocomposites synthesized from PbTe nanocrystals", **J. Martin**, **G.S. Nolas**, W. Zhang and L. Chen Appl. Phys. Lett. 90, 222112 (2007).
 19. "Transport Properties of Thermoelectric Nanocomposites", **L.M. Woods**, A. Popescu, **J. Martin**, and **G.S. Nolas**, Proc. Mater. Rec. Soc. 1166 (2009) in press.
 20. "Enhanced thermoelectric properties in PbTe nanocomposites", H. Kirby, **J. Martin**, **A. Datta**, L. Chen, **G.S. Nolas**, Proc. Mater. Rec. Soc. 1166 (2009) in press.

Conference Presentations (contributed) [2008-09]:

1. "Origin of glass-like relaxation in Fe₃O₄ ferrofluids" **M. Morales**, M. Phan, **S. Pal** and **H. Srikanth**, 2009 INTERMAG Conference, Sacramento CA (May 4-8, 2009)
2. "Magnetic frustration and particle size effects in nanostructured gadolinium iron garnets" M. H. Phan, **M. B. Morales**, C. N. Chinnasamy, B. Latha, V. G. Harris and **H. Srikanth**, 2009 INTERMAG Conference, Sacramento CA (May 4-8, 2009)
3. "Origin of magnetic anomalies and relaxation mechanisms in ferrofluids" **M. B. Morales**, M. H. Phan, N. A. Frey, **S. Pal** and **H. Srikanth**, 2009 APS March Meeting, Pittsburgh, PA (March 16-20, 2009)
4. "Competing effects of blocking and spin frustration in nanostructured gadolinium iron garnets" M. H. Phan, **M. B. Morales**, **H. Srikanth**, C. N. Chinnasamy and V. G. Harris, 2009 APS March Meeting, Pittsburgh, PA (March 16-20, 2009)
5. "Functional nanocomposite polymer films with uniform nanoparticle dispersions" –K. Stojak, **S. Pal**, M. J. Miner, **H. Srikanth**, S. Skidmore, J. Wang and T. Weller, 2009 APS March Meeting, Pittsburgh, PA (March 16-20, 2009)
6. "Magnetic transitions and giant magnetocaloric effect in EuGaGe clathrates" –**A. Chaturvedi**, S. Stefanoski, M. H. Phan, G. T. Woods, **G. S. Nolas** and **H. Srikanth**, 2009 APS March Meeting, Pittsburgh, PA (March 16-20, 2009)
7. "Anomalous magnetism and exchange bias in coupled Au-Fe₃O₄ nanoparticles" –N. A. Frey, M. H. Phan, S. Srinath, C. Wang, S. Sun and **H. Srikanth** –2008 MRS Fall meeting, Dec. 1-5, 2008 (Boston, MA)
8. "Origin of magnetic anomalies in the liquid, frozen and mixed states of ferrofluids" –M. H. Phan, **M. B. Morales**, **S. Pal**, N. A. Frey and **H. Srikanth** –53rd annual MMM conference, Nov. 10-14, 2008 (Austin, TX)

9. “Magnetization dynamics and magnetocaloric effect in nanostructured $Gd_3Fe_5O_{12}$ garnets” –M. Phan, **M. B. Morales**, **H. Srikanth**, C. N. Chinnasamy and V. G. Harris –53rd annual MMM conference, Nov. 10-14, 2008 (Austin, TX)
10. “Synthesis and magnetic properties of gold-coated core-shell $Au@Fe_3O_4$ nanoparticles” – **S. Pal**, **M. B. Morales**, M. H. Phan, **P. Mukherjee** and **H. Srikanth** –53rd annual MMM conference, Nov. 10-14, 2008 (Austin, TX)
11. “Synthesis of surface functionalized magnetic nanoparticles and their polymer composites” –M. J. Miner, **S. Pal**, K. Stojak, **H. Srikanth**, S. Skidmore, J. Wang and T. Weller –53rd annual MMM conference, Nov. 10-14, 2008 (Austin, TX).
12. “Growth of nanoparticle coatings of $Ca_3Co_4O_9$ by a microwave plasma process”, **Ted Wangenstein**, **Marek Merlak**, **Pritish Mukherjee**, and **Sarath Witanachchi**, presented at the 2009 spring Materials Research Society Meeting, April 2009, San Francisco, CA.
13. “A new method for forming surfactant-free PbSe quantum dot films and quantum dot-polymer composites for excitonic solar cells”, **G. Dedigamuwa**, D. Ferizovic, M. Munoz, **P. Mukherjee** and **S. Witanachchi**, presented at the 2009 spring Materials Research Society Meeting, April 2009, San Francisco, CA.
14. “Growth of epitaxial $ZnO:Mn/ZnO:V$ heterostructures and ferroelectric-ferromagnetic characterization”, **D. Mukherjee**, **T. Dhakal**, **R. Hyde**, **P. Mukherjee**, **H. Srikanth**, and **S. Witanachchi**, presented at the 2009 spring Materials Research Society Meeting, April 2009, San Francisco, CA.
15. “Growth of epitaxial $CoFe_2O_4/PZT$ heterostructures and ferroelectric-ferromagnetic characterization”, **D. Mukherjee**, **T. Dhakal**, **R. Hyde**, **P. Mukherjee**, **H. Srikanth**, and **S. Witanachchi**, presented at the 2008 Fall Materials Research Society Meeting, December 2008, Boston, MA.
16. “Enhanced Power Factor in Nanocomposite Materials and Magnetocaloric Materials”, **G.S. Nolas**, Invited, 8th Pacific Rim Conference on Ceramic and Glass Technology (PacRim8), Vancouver, Canada, May 31 – June 5, 2009.
17. “Enhanced thermoelectric properties of PbTe nanocomposites”, **J. Martin**, L. Wang, L. Chen and **G.S. Nolas**, presented at the 27th International Thermoelectrics Conference, Corvallis, OR, August 7, 2008.
18. “Transport Properties of Lead Chalcogenide Nanocomposites”, **G.S. Nolas**, **J. Martin**, S. Stefanoski, L. Wang and L. Chen, presented at the American Physical Society March Meeting, New Orleans, LA, March 13, 2008.

Invited talks

1. **H. Srikanth**, International Conference on Materials for Advanced Technologies (ICMAT 2009), Singapore (June 2009)
2. **H. Srikanth**, US-Indo Technology Forum on “New Directions and Novel Applications in Magnetism”, Mumbai, India (March 1 – 4, 2009)
3. **H. Srikanth**, Workshop on Magnetic Nanomaterials, S. N. Bose Center for Basic Sciences, Kolkata, India (January 26-28, 2009)
4. **H. Srikanth**, Defense Sciences Research Council (DSRC –a division of DARPA) sponsored ‘Advanced Materials for Enhanced Passive Components’ Workshop, Oct. 30-31, 2008
5. **H. Srikanth**, Condensed Matter Seminar, Department of Physics, University of Delaware, Newark, DE (October 14, 2008)

6. **H. Srikanth**, Center for Integrated Electronics Seminar, Department of ECE, Rensselaer Polytechnic Institute, Troy, NY (October 1, 2008)
7. **H. Srikanth**, Novel Trends in Magnetic Materials for Electromagnetic Applications Workshop, Santorini, Greece (September 3 – 5, 2008)

Patent Pending

1. **G.S. Nolas**, “Bulk Dimensional Nanocomposites for Thermoelectrics Applications”, Patent Pending, US Provisional Patent Application # 12/104,016, filed April 2, 2009.

Other noteworthy professional activities by CIFM researchers:

- CIFM supported graduate student Marienette Morales defended her Master’s thesis in May 2009 and received her M.S. degree
- Hari Srikanth selected to co-organize symposium on ‘Functional oxide nanostructures and heterostructures’ at the 2010 MRS Spring Meeting in April 2010 in San Francisco
- Hari Srikanth served as a Program Committee member and Publication Editor for the annual Magnetism and Magnetic Materials (MMM) conference held in Austin, TX in Nov. 2008. He continues to serve as a publication editor for the 2010 joint MMM/Intermag conference in January 2010 in Washington DC

IV. Conclusion

Update on Milestones:

- * Design and fabrication of lithographically patterned metallic microwires: Work currently in progress. Expect completion by January 2010.
- * PLD growth of ferroelectric/ferrite heterostructures with controlled interface strain, RF and microwave measurements of polymer composites and oxide films : The growth and characterization of epitaxial PZT/CFO and ZnO:Mn/ZnO:V heterostructures by PLD was completed in July 2009. RF and microwave measurements are ongoing and will be completed in the next two quarters.
- * Functionalization of ferrofluids with biocompatible surfactant coatings of the nanoparticles. Chemical and physical properties characterization of the functionalized ferrofluids: Completed in July 2009.
- * Structural, electrical, and capacitive measurements on nanotube networks: Structural measurements completed August 2009. Electrical and impedance measurements are ongoing and expected to be completed by March 2010.
- * Integration of nanoparticles with polymer and characterization for optical properties: Completed in June 2009.
- * Comparative studies and analysis - Synthesis bulk materials for comparison to the nano-scale TE materials: Completed in August 2009.

Relevance of the Research:

From the perspective of military applications specific to the US Army Medical Research and the DoD in general, we have identified three key targeted applications where timely advances are critically needed. The concerted effort in this Integrated Functional Materials Project and our ongoing development of an interdisciplinary Center for Integrated Functional Materials (CIFM) at USF will advance the science knowledge base in these areas. The three targeted tasks broadly encompass issues of most importance to the soldier in the battlefield. At the culmination of the projects specific advances are expected in new materials and functionalities that aid in diagnostics and communication of medical problems encountered by the soldier in the field, sensors with improved sensitivity and specificity to detect threats such as trace biological agents, and the need for novel portable and renewable energy and power sources to power these new devices.

Once established, CIFM will continue to be a national resource in the development of new materials and devices for the military and commercial sector, and a stimulant of industry in the United States based on emerging technologies and manufacturing processes. The specific outcome of the research activities is therefore expected to lead to new devices/systems/composite materials useful for the USAMRMC.

V. Bibliography

1. S. Odenbach, "Recent progress in magnetic fluid research", *Journal of Physics: Condensed Physics* **16**, R1135 (2004).
2. Phan M. H. and Peng H. X., "Giant Magneto-impedance Materials: Fundamentals and Applications", *Progress in Materials Science* **53**, 323 2008.
3. Kurlyandskaya G. V., Sánchez M. L., Hernando B., Prida V. M., Gorria P., and Tejedor M., "Giant-magnetoimpedance-based sensitive element as a model for biosensors", *Applied Physics Letters* **82**, 3053 (2003).
4. Chiriaca H., Herea D. D., Corodeanu S., "Microwire array for giant magneto-impedance detection of magnetic particles for biosensor prototype", *Journal of Magnetism and Magnetic Materials* **311**, 425 (2007).
5. Kumar A., Mohapatra S., Fal-Miyar V., Cerdeira A., García J. A., Srikanth H., Gass J., Kurlyandskaya G. V., "Magnetoimpedance biosensor for Fe₃O₄ nanoparticle intracellular uptake evaluation", *Applied Physics Letters* **91**, 143902 (2007).
6. Collins P.G., Zettl A., Bando H., Thess A. and Smalley R. E., *Science* **278** 100-03, 1997.
7. Rinkio M., Johansson A., Paroanu G. S. and Törmä P., *Nano Lett.* **9**, 643-47, 2009.
8. Kong J., Franklin N. R., Zhou C., Chapline M. G., Peng S., Cho K., Dai H., *Science* **287** 622-25, 2000.
9. Tans S. J., Devoret M. H., Dai H., Thess A., Smalley R. E., Geerligs L. G., Dekker C., *Nature* **386** 474-77, 1997.
10. Treacy M. M. J., Ebbesen T. W., Gibson J. M., *Nature* **381** 678-80, 1996.
11. Planeix J. M., Coustel N., Coq B., Brotons V., Kumbhar P. S., Dutartre R., Geneste P., Bernier P. and Ajayan P. M., *J. Am. Chem. Soc.* **116** 7935-36, 1994.
12. Kim C., Kim Y. A., Kim J. H., Kataoka M. and Endo M., *Nanotechnology* **19** 145602 (1-5), 2008.
13. Kornev K. G., Halverson D., Korneva G., Gogotsi Y. and Friedman G., *Appl. Phys. Lett.* **92** 233117(1-3), 2008.
14. Gupta A. K. and Gupta M., *Biomaterials* **26** 3995-4021, 2005.
15. Lu F., Gu L., Meziani M. J., Wang X., Luo P. G., Veca L. M., Cao L. and Sun Y.-P., *Adv. Mater.* **21** 139-52, 2009.
16. Korneva G., Ye H., Gogotsi Y., Halverson D., Friedman G., Bradley J-C. and Kornev K. G., *Nano Lett.* **5** 879-84, 2005.
17. Sun S, and Zeng H., *J. Am, Chem. Soc.* **124** 8204-05, 2002.
18. Miller S. A., Young V. Y. and Martin C. R., *J. Am. Chem. Soc.* **123** 12335-42, 2001.
19. Majetich S. A. and Sachan M., *J. Phys. D: Appl. Phys.* **39** R407-22, 2006.
20. Likodimos V., Glenis S., Guskos N. and Lin C. L., *Phys. Rev. B.* **68** 045417(1-6), 2003.
21. S. Pal, S. Chandra, M. -H. Phan, P. Mukherjee and H. Srikanth, *Nanotechnology* (in press, 2009).
22. J. Kim, J. E. Lee, S. H. Lee, J. H. Yu, J. H. Lee, T.G. Park and T. Hyeon, *Advanced materials*, **20**, 478, 2008.
23. A. Wijaya and K. Hamad-Schifferli, *Langmuir*, **23**, 9546, 2007.

24. J. Xie, C. Xu, N. Kohler, Y. Hou and S. Sun; *Advanced materials*, **19**, 3163, 2007.
25. J. H. Yin, J. Ding, B. H. Liu, J. B. Yi, X. S. Miao and J. S. Chen, *Journal of Applied Physics*, **101**, 09K509, 2007.
26. Alex Goldman, *Modern Ferrite Technology* 2nd Edition, Springer, New York, 2006.
27. R. M. Bozorth, Elizabeth F. Tilden, and Albert J. Williams, *Phys. Rev.* **99**, 1788, 1955.
28. P. D. Thang, G. Rijnders, D. H. A. Blank, *J. of Magnetism and Magnetic Materials* **310**, 2621, 2007.
29. I. C. Noyan, J. B. Cohen, *Residual Stress*, Springer-Verlag, 1987.
30. S.R. Murthy, *Cryst. Res. Technol.* **25**, 4, 461, 1990.
31. H. Srikanth, J. Wiggins, and H. Rees, *Rev. of Sci. Inst.* **70**, 3097, 1999.
32. N. A. Frey, S. Srinath, and H. Srikanth, M. Varela and S. Pennycook, G. X. Miao and A. Gupta, *Phys. Rev. B* **74**, 024420, 2006.
33. P. Poddar, J. L. Wilson, H. Srikanth, D. F. Farrell, and S. A. Majetich, *Phys. Rev. B* **68**, 214409, 2003.
34. G. T. Woods, P. Poddar, H. Srikanth, and Ya. M. Mukovskii, *J. Appl. Phys.* **97**, 10C104, 2005.
35. A. Aharoni, E. H. Frei, S. Shtrikman, and D. Treves, *Bull. Res. Council. Isr., Sect. F* **6A**, 215, 1957.
36. L. Spinu, H. Srikanth, A. Gupta, X. W. Li, and G. Xiao, *Phys. Rev. B* **62**, 8931, 2000.
37. F.W. Smith, *Physical Review B*, **14**, 241, 1976.
38. Y. C. Yang, C. Song, X.H. Wang, F.Zeng, and F. Pan, *Appl. Phys. Lett.* **92**, 012907, 2008.
39. Y. C. Yang, C. Song, F. Zeng, and F. Pan, Y. N. Xie, T. Liu, *Appl. Phys. Lett.* **90**, 242903, 2007.
40. Hugo E. Romero and Marija Drndic, *Phys. Rev. Lett.*, **95** 156801, 2005.
41. Dehu Cui, Jian Xu, Ting Zhu, Gray Paradee, and S. Ashok, *Appl. Phys. Lett.*, **88**, 183111, 2006.
42. A. N. Aleshin, S. R. Williams, A. J. Heeger, *Synth. Met.* **94**, 173, 1998.
43. A. Nozik, *Chemical Physical Letters*, **457**, 3-11, 2008.
44. Martin, J., Nolas, G. S. Zhang, W., and Chen, L., *App. Phys. Lett.*, **90**, 222112, 2007.
45. Martin, J., Wang, L., Chen, L., and Nolas, G. S., *Phys. Rev. B*, **79**, 115311, 2009.
46. Nolas, G. S., Sharp, J., and Goldsmid, H. J., *Thermoelectrics Basic Principles and New Materials Developments* (New York: Springer), 2001.
47. Poudel, B., Hao, Q., Ma, Y., Lan, Y. C., Minnich, A., Yu, B., Yan, X., Wang, D. Z., Muto, A., Vashaee, D., Chen, X. Y., Liu, J. M., Dresselhaus, M. S., Chen, G., and Ren, Z. F., *Science*, **320**, 634, 2008.
48. Sofo, J. O., and Mahan, J. D., *Phys. Rev. B*, **58**, 15620, 1998.
49. Popescu, A., Woods, L. M., Martin, J., and Nolas, G. S., *Phy. Rev. B*, **79**, 205302, 2009.
50. Vafayi, K., Calandra, M., and Gunnarsson, O., *Phys. Rev. B*, **74**, 235116, 2006.
51. Srivastava, G. P., *The Physics of Phonons* (Adam Hilger, Bristol), 1990.
52. Hyun, D. B., Oh, T. S., Hwang, J. S., Shim, J. D., and Kolomoets, N. V., *Scr. Mater.*, **40**, 49, 1999.
53. Yamashita, O., Tomiyoshi, S., and Makita, K. J., *Appl. Phys.*, **93**, 368, 2003.